ELSEVIER

Contents lists available at ScienceDirect

## Computers and Fluids

journal homepage: www.elsevier.com/locate/compfluid



# The performance of subgrid-scale models in large-eddy simulation of Langmuir circulation in shallow water with the finite volume method

Seyedmohammadjavad Zeidi, L. Srujana Sarvepalli, Andrés E. Tejada-Martínez

Department of Civil & Environmental Engineering, University of South Florida, 4202 East Fowler Avenue ENC 3300, Tampa, FL 33620, USA

#### ARTICLE INFO

### Keywords: Langmuir circulation Large-eddy simulation Subgrid-scale modeling Coastal ocean Turbulence

#### ABSTRACT

Langmuir turbulence consists of Langmuir circulation (LC) generated at the surface of rivers, lakes, bays, and oceans by the interaction between the wind-driven shear and surface gravity waves. In homogeneous shallow water, LC can extend to the bottom of the water column and interact with the bottom boundary layer. Large-eddy simulation (LES) of LC in shallow water was performed with the finite volume method and various forms of subgrid-scale (SGS) model characterized by different near-wall treatments of the SGS eddy viscosity. The wave forcing relative to wind forcing in the LES was set following the field measurements of full-depth LC during the presence of LC engulfing a water column 15 m in depth in the coastal ocean, reported in the literature. It is found that the SGS model can greatly impact the structure of LC in the lower half of the water column. Results are evaluated in terms of (1) the Langmuir turbulence velocity statistics and (2) the lateral (crosswind) length scale and overall cell structure of LC. LES with an eddy viscosity with velocity scale in terms of S and  $\Omega$  (where S is the norm of the strain rate tensor and  $\Omega$  is the norm of the vorticity tensor) and a Van Driest wall damping function (referred to as the S-Omega model) is found to provide best agreement with pseudo-spectral LES in terms of the lateral length scale and overall cell structure of LC. Two other SGS models, namely the dynamic Smagorinsky model and the wall-adapting local-eddy viscosity model are found to provide less agreement with pseudospectral LES, for example, as they lead to less coherent bottom convergence of the cells and weaker associated upward transport of slow downwind moving fluid. Finally, LES with the S-Omega SGS model is also found to lead to good agreement with physical measurements of LC in the coastal ocean in terms of Langmuir turbulence decay during periods of surface heating.

### 1. Introduction

Turbulence at the surface of oceans, lakes, bays, and rivers is generated by a combination of surface winds, surface wave breaking, wave-current interaction and surface heat fluxes. Wave-current interaction gives rise to Langmuir turbulence, characterized by a wide range of Langmuir circulation (LC) scales, parallel counter-rotating vortices or cells roughly aligned in the direction of the wind (Fig. 1a). Wind speeds greater than approximately 3 m s<sup>-1</sup> and winds roughly parallel to waves provide favorable conditions for the generation of Langmuir turbulence. Generated at the surface at centimeter scales, the cells grow in depth and width up to tens of meters, typically engulfing the mixed layer in the upper ocean [1] or the entire water column in homogenous shallow water [2] on the order of tens of minutes. The more permanent, larger LC scales manifest by accumulating bubbles, particulate matter and flotsam along their surface convergence zones, forming what are often referred

to as "windrows" (Fig. 1).

A common sketch of LC vortex pairs is shown in Fig. 1. The surface convergence of each cell leads to a downwelling region characterized by negative vertical velocity fluctuations (w'), while the bottom convergence leads to an upwelling region characterized by positive w'. These upwelling and downwelling limbs of LC induce non-local vertical transport of momentum, turbulent kinetic energy (TKE), and scalars, ultimately leading to enhanced levels of vertical mixing [3]. A key characteristic of LC is that its downwelling limbs coincide with regions of positive downwind velocity fluctuations, as the cells entrain high-speed downwind moving fluid into the water column. Thus, the cells lead to an enhanced downwind mean current coinciding with the downwelling limbs (Fig. 1). Analogously, the upwelling limbs of the cell transport slow downwind moving fluid towards the surface.

Historically, Langmuir cells have been measured within the upper ocean surface mixed layer in deep water. However, there have been

E-mail address: aetejada@usf.edu (A.E. Tejada-Martínez).

<sup>\*</sup> Corresponding author.

various field measurements of Langmuir cells in shallow coastal shelf environments, where under neutrally or weakly stratified conditions the cells reach the bottom of the water column and interact with the bottom boundary layer. Gargett et al. [2] and Gargett and Wells [4] reported measurements of Langmuir cells engulfing an entire water column 15 m in depth on the inner shelf off the coast of southern New Jersey, undergoing strong wind and wave forcing during the passage of a storm. These supercells persisted for over 18 h. Full-depth Langmuir cells have also been measured at a deeper site of approximately 26 m depth on mid-shelf off the coast of Georgia [5–7]. Kukulka et al. [8,9] highlighted coastal Langmuir cells in a weakly stratified water column 16 m in depth measured during the Coupled Boundary Layers and Air-Sea Transfer Experiment in Low Winds (CBLAST-Low) off the coast of Massachusetts [10,11].

Gargett et al. [2] denoted their observed full-depth cells as Langmuir supercells (LS) due to their significant impact on the turbulence dynamics throughout the entire water column and the cells' distinct structure compared to the more common LC in the upper ocean mixed layer. The full-depth cells lead to a Langmuir turbulence regime with characteristics vastly different than classical shear-driven turbulence. Furthermore, Gargett et al. [2] and Gargett and Wells [4] established LS as an important mechanism in the resuspension and subsequent horizontal transport of sediment and bioactive material on shallow shelves.

Although large-eddy simulations (LES) of full-depth LC in inner coastal shelves following the previously discussed field measurements have proven successful, these simulations have been limited to pseudospectral solvers employing highly accurate spectral discretizations in the horizontal directions (e.g. see Deng et al. [12,13], Tejada-Martinez and Grosch [14], Kukulka et al. [8,9] and Shrestha et al. [15,16]). To allow for simulations of LC affected by lateral boundaries typical of coastal, lake and estuarine zones, it would be beneficial to extend LC-resolving simulations to non-spectral discretizations capable of handling complex geometry. As an initial step towards that end, in this manuscript, a second-order accurate finite volume discretization is employed to perform LES of full-depth LC with different subgrid-scale (SGS) models.

While immersed boundary methods offer an effective approach for incorporating complex boundaries into spectral simulations, our focus on the finite volume method (FVM) is driven by its widespread application and the availability of well-developed FVM-based solvers, such as Fluent and openFoam (Fluent [17]; Weller et al. [18]). This choice is further substantiated by our specific interest in evaluating the SGS models' performance, particularly in the context of eddy viscosity modifications near the wall, which have been well-established within

the conventional FVM approach [19].

The pseudo-spectral LES of Tejada-Martinez and Grosch [14] showed that the full-depth Langmuir cells can contribute between 50 and 80 % of the TKE throughout the water column. Furthermore, the cells can increase the peak TKE value by about 70 % in the bottom boundary layer. This is due to the bottom convergences of the cells which induce elevated values of crosswind velocity variance and due to the dowelling limbs of the cells which induce elevated values of the downwind velocity variance. As the downwelling limbs of the cells impinge on the bottom they cause a thinning of the bottom boundary layer. This thinning induces elevated values of the downwind velocity variance (i.e. elevated shear turbulence). Thus, careful consideration must be given to the extension of LES of full-depth LC to a less accurate method such as finite volumes and to the SGS model in their representation of this magnified turbulence regime relative to classical shear turbulence.

The principal goal of this study is to assess the performance of various SGS models in LES of full-depth LC with the FVM on a fixed mesh commensurate of wall modeled LES [20–22]. Considering the influence of full-depth LC on the bottom boundary layer, focus is placed on the SGS models and their different near-wall treatments of the eddy viscosity. The assessment is made with respect to pseudo-spectral LES, in terms of the resolved full-depth LC structure and turbulence diagnostics such as resolved mean velocity and velocity variances. The pseudo-spectral LES has been found to provide results consistent with field measurements of LC [2,4,14,23].

The progression of the manuscript is as follows. First in Section 2, the filtered Navier-Stokes equations with the Craik-Leibovich (C-L) vortex force [24] are presented. The C-L vortex force accounts for the wave-current interaction mechanism that generates LC. In Section 3, the SGS models tested are presented and in Section 4 the computational domain, boundary conditions and grids employed for the LES are described. Section 5 presents results of the finite volume LES obtained with the different SGS models and compares them to pseudo-spectral LES results. In this section, LES with the S-Omega SGS model is identified as performing in closest agreement with the pseudo-spectral LES in terms of (1) the Langmuir turbulence velocity statistics and (2) the lateral (crosswind) length scale and overall cell structure of LC.

Recent LES and field measurements have begun to shed light on the influence of other coastal ocean processes on full-depth LC such as tidal forcing [8,15] and surface heat fluxes [25]. In Section 5, an additional test of finite volume LES with the S-Omega SGS model is presented consisting of full-depth LC under the influence of surface heat fluxes. Good agreement with the physical measurements of LC of Gargett [25] is

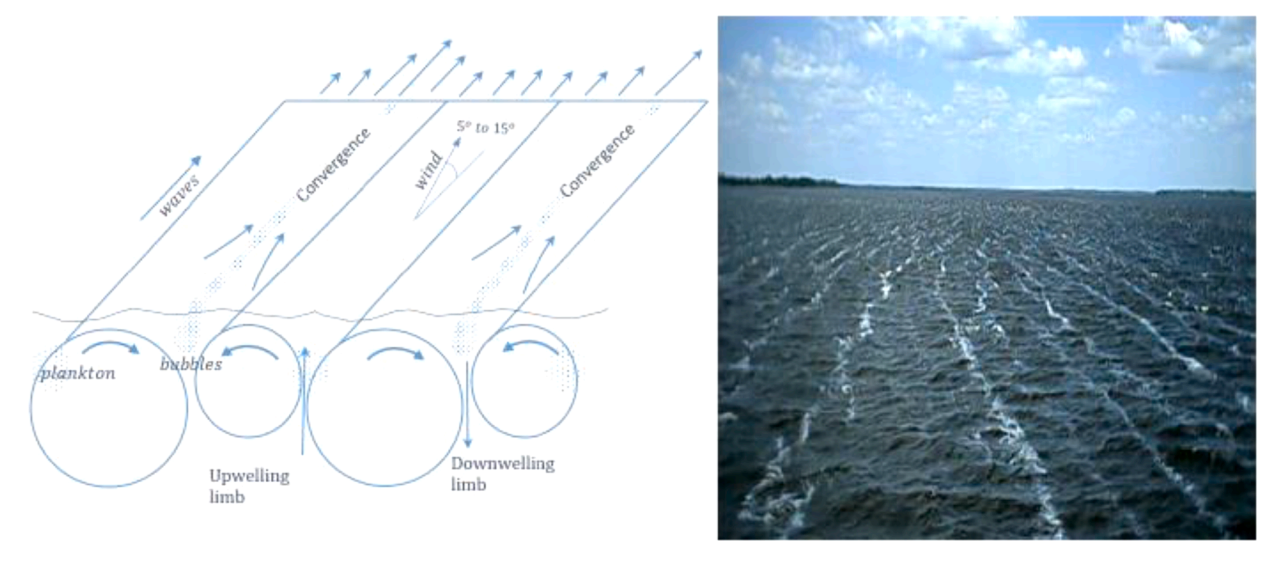


Fig. 1. Sketch of LC (left) and photograph of windrows along the surface convergence of LC in Ochlockonee Bay, Florida (right). Note the lateral meandering and y-junctioning exhibited by the windrows in the field. Photograph source: ldeo.columbia.edu/~ant/Langmuir.

found in terms of Langmuir turbulence decay during periods of surface heating.

Finally, Section 6 presents a summary of the results and discusses future research.

## 2. Navier-Stokes equations and the Craik-Leibovich vortex force

Phase-averaging of surface gravity waves gives rise to the C-L vortex force [24] in the Navier-Stokes equations. These equations admit LC without the need to resolve surface deformation due to waves as the wave-current interaction that generates LC is accounted for though the C-L vortex force. The incompressible spatially filtered continuity equation, the Navier-Stokes equations under the Boussinesq approximation augmented with the C-L vortex force, and the energy or temperature equations are

$$\frac{\partial \overline{u}_i}{\partial x_i} = 0 \tag{1}$$

$$\frac{\partial \overline{u}_{i}}{\partial t} + \overline{u}_{j} \frac{\partial \overline{u}_{j}}{\partial x_{j}} = -\frac{1}{\rho_{0}} \frac{\partial \overline{\Pi}}{\partial x_{i}} + \nu \frac{\partial^{2} \overline{u}_{i}}{\partial x_{j}^{2}} + \frac{\partial \tau_{ij}}{\partial x_{j}} + \beta (\overline{T} - T_{0}) \delta_{i3} \mathbf{g} + \epsilon_{ijk} U_{j}^{s} \overline{\omega}_{k}$$
(2)

$$\frac{\partial \overline{T}}{\partial t} + \overline{u}_j \frac{\partial \overline{T}}{\partial x_i} = \kappa \frac{\partial^2 \overline{T}}{\partial x_i^2} + \frac{\partial \lambda_j}{\partial x_i}$$
(3)

respectively, where the over-bar denotes application of the filter,  $\overline{u}_i$  is the filtered velocity,  $\overline{T}$  is the filtered temperature,  $\overline{\Pi}$  is a filtered modified pressure,  $\tau_{ij}$  is the deviatoric portion of the subgrid-scale (SGS) stress generated by the spatial filtering [26] (with the isotropic part lumped into the pressure (not shown)), and  $\lambda_j$  is the SGS heat flux. Furthermore,  $\rho_0$  is the fluid density and  $\nu$  its kinematic viscosity,  $T_0$  is a reference temperature,  $\beta$  is the coefficient of thermal expansion and  $\kappa$  is diffusivity.

Eqs. (1) and (2) are defined in a Cartesian coordinate system consisting of streamwise (or downwind)  $(x_1)$ , spanwise (or crosswind)  $(x_2)$ , and vertical (or wall-normal)  $(x_3)$  directions. In (2), the gravitational acceleration is g with the gravity vector pointing in the  $-x_3$  direction.

The last term in (2) is the C-L vortex force consisting of the cross product between the Stokes drift velocity  $U_j^s$ , induced by the surface gravity waves, and the filtered vorticity  $\overline{\omega}_k$ . In this term,  $\epsilon_{ijk}$  is the Levi-Civita epsilon. The modified filtered pressure in (2) is defined as

$$\overline{\Pi} = \frac{\overline{p}}{\rho} + \frac{1}{2} \left[ U_i^s U_i^s + 2u_i U_i^s \right] \tag{4}$$

where  $\overline{p}$  is the filtered pressure under the Boussinesq approximation. In this study, the Stokes drift velocity is taken to be aligned in the direction of the wind, therefore, the crosswind and vertical components of the Stokes drift are zero ( $U_2^S=U_3^S=0$ ). The downwind component is taken

$$U_1^S = \sigma k a^2 \frac{\cosh(2kx_3)}{2\sinh^2(kH)} \tag{5}$$

defined by Phillips. In (5) H is the depth of the water column,  $\sigma$  is the dominant frequency, k is the dominant wavenumber and a is the dominant amplitude of the waves generating LC. The wavenumber and the frequency can be related through the surface gravity wave dispersion relation. Furthermore, the dominant wavelength and period of the waves can be obtained through  $\lambda = 2\pi/k$  and  $T = 2\pi/\sigma$ , respectively.

## 3. SGS stress models

The performance of various SGS stress models will be investigated in LES of shallow water wind-driven shear flow in which the turbulence is characterized by full-depth LC. In this setting, the LC is generated at the surface growing in time over crosswind and depth extents, eventually reaching the bottom of the water column and remaining in equilibrium

for the rest of the simulation. As such, the LES SGS stress model should not cause excessive damping of resolved scales which could lead to inaccurate equilibrium turbulence dynamics and final crosswind width of the cells. However, it is well known that classical SGS stress models, such as the Smagorinsky model, can cause excessive turbulence damping. Thus, various forms of the Smagorinsky model will be tested, characterized by different near wall treatments.

Following the Boussinesq hypothesis, the deviatoric portion of the SGS stress in Eq. (1) is expressed in terms of the eddy viscosity  $\nu_t$ 

$$\tau_{ii} = \nu_t \overline{S}_{ii} \tag{6}$$

where the filtered symmetric part of the velocity gradient or the filtered strain rate tensor is defined as

$$\overline{S}_{ij} \equiv \frac{1}{2} \left( \frac{\partial \overline{u}_i}{\partial x_i} + \frac{\partial \overline{u}_j}{\partial x_i} \right) \tag{7}$$

The SGS heat flux,  $\lambda_j$ , in Eq. (3) is modeled via an eddy diffusivity taken as  $\nu_t/Pr_t$  times the filtered temperate gradient,  $\partial \overline{T}/\partial x_i$ , where the turbulent Prandtl number is set as  $Pr_t = 0.85$ .

#### 3.1. Wall adapting Smagorinsky model

The simplest model that could be considered is the Smagorinsky model in which the Smagorinsky length scale is integrated within a spatially varying mixing length scale as follows:

$$\nu_t = L_m^2 |\overline{S}| \tag{8}$$

where  $|\overline{S}| \equiv (2\overline{S}_{ij}\overline{S}_{ij})^{1/2}$  is the norm or absolute value of the filtered strain rate and  $L_m$  is the spatially varying mixing length scale computed as

$$L_m = \min(\kappa d_{wn}, C_S \Delta) \tag{9}$$

In the previous expression  $d_{wn}$  is the wall distance normal to the wall,  $\Delta$  is the local grid scale given as the cube root of the cell volume,  $\kappa=0.41$  is the von Karman constant, and  $C_S=0.1$  is the Smagorinsky constant. Away from a wall,  $L_m$  is determined through the length scale  $C_S\Delta$ . Near the wall,  $L_m$  is dominated by  $d_{wn}$ , as in this region the energetic eddies of the turbulence scale with  $d_{wn}$ . This near-wall behavior follows the Reynolds-averaged Prandtl's mixing-length theory.

Shur et al. [19] showed that the Smagorinsky model above can result in excessive dissipation in the outer layer of turbulent channel flow and proposed a mixing length scale,  $L_m$ , accounting for grid anisotropy and modified by a van Driest wall damping function [27]:

$$\nu_{t} = \min\left[\left(\kappa d_{wall}\right)^{2}, \left(C_{Smag}\Delta\right)^{2}\right] \left|\overline{S}\right| \left\{1 - \exp\left[-\left(y^{+}/25\right)^{3}\right]\right\}$$
 (10)

where the wall damping function is defined in terms of  $y^+$ , the wall distance normal to the wall in plus (or wall) units. The latter is defined as  $y^+ = u_* d_{wall} / \nu$  where  $u_*$  is the wall friction velocity. The mixing length scale,  $L_m$ , is modified through the local grid scale as follows:

$$\Delta = \min(\max(C_{wall} \ d_{wall}, \ C_{wall} \ h_{max}, \ h_{wn}), h_{max}) \tag{11}$$

where  $C_{wall}=0.15$ ,  $h_{wn}$  is the grid cell size in the wall-normal direction, and  $h_{max}$  is the maximum local grid spacing (i.e., the maximum edge length of the cell). Note that the outer layer is the region extending from the edge of the inner layer (or logarithmic layer) to the outer edge of the boundary layer itself, where the flow velocity approaches the free stream velocity.

## 3.2. Wall adapting S-Omega model

A drawback of the wall adapting Smagorinsky model is that it yields non-zero eddy viscosity in regions of constant shear. Consequently, the model results in excessive values of the eddy viscosity in flows characterized by transition to turbulence. The model can also result in excessively high eddy viscosity in flows with separated shear layers. To alleviate these inaccuracies, the norm or the magnitude of the filtered strain rate tensor can be replaced by the absolute value of the norm of the filtered strain rate tensor minus the norm of the filtered vorticity tensor as proposed in [17]:

$$\nu_{t} = \min\left[\left(\kappa d_{walt}\right)^{2}, \left(C_{Smag}\Delta\right)^{2}\right] \text{ abs}(|\overline{S}| - |\overline{\Omega}|) \left\{1 - \exp\left[-\left(y^{+}/25\right)^{3}\right]\right\}$$
(12)

where  $\Delta$  is given in (11),  $|\overline{\Omega}| \equiv (2\overline{\Omega}_{ij}\overline{\Omega}_{ij})^{1/2}$  and

$$\overline{\Omega}_{ij} \equiv \frac{1}{2} \left( \frac{\partial \overline{u}_i}{\partial x_j} - \frac{\partial \overline{u}_j}{\partial x_i} \right) \tag{13}$$

is the anti-symmetric part of the resolved velocity gradient or the resolved vorticity tensor.

## 3.3. Dynamic Smagorinsky model

A third model tested is the dynamic Smagorinsky model [28] in which the eddy viscosity is taken as

$$\nu_t = (C_S \Delta)^2 |\overline{S}| \tag{14}$$

where the Smagorinsky coefficient is calculated dynamically as a function of space and time. The dynamic computation of the coefficient relies on the resolved Leonard tensor defined as

$$L_{ij} = \widehat{\overline{u_i}} \overline{u_i} - \widehat{\overline{u}_i} \widehat{\overline{u}_j}$$
 (15)

where the over-hat notation denotes application of a spatial filter, often referred to as the test filter.

Note that the Leonard tensor  $L_{ij}$  may computed exactly via the resolved velocity  $\overline{u}_i$  in (15) and can also be approximated via the Smagorinsky model and minimization of the difference between this approximation and the definition in (15) leads to the dynamic expression for the Smagorinsky coefficient:

$$C_S^2 = \frac{\left\langle \left( L_{ij} - L_{kk} \ \delta_{ij} / 3 \right) M_{ij} \right\rangle}{\left\langle M_{ij} M_{ij} \right\rangle} \tag{16}$$

where  $\delta_{ii}$  is the Kronecker delta and

$$M_{ij} = -2\left(\widehat{\Delta}^{2} | \widehat{\overline{S}} | \widehat{\overline{S}}_{ij} - \Delta^{2} | \widehat{\overline{S}^{i}} | \overline{S}_{ij}\right)$$

$$(17)$$

In the above equation,  $\Delta$  is the width of the primary filter applied to obtain the filtered Navier-Stokes equations in (2) and  $\widehat{\Delta}$  is the width of the filter resulting from sequential application of the primary filter and the test filter. In implicit LES,  $\Delta$  is taken as the local grid scale (i.e. the cube root of the cell volume) with  $\widehat{\Delta}=2\Delta$ . Finally, the brackets in the numerator and denominator in the expression for  $C_S^2$  denote local averaging performed for stability.

## 3.4. Wall adapting local eddy viscosity (WALE) model

As the distance to a wall  $(d_{wn})$  approaches zero, the norm of the filtered strain rate,  $|\overline{S}|$ , is O(1) and thus in this limit the eddy viscosity in Eq. (14) is  $\nu_t \sim O(1)$ ; however, the proper wall scaling is  $\nu_t \sim O\left(d_{wn}^3\right)$  [29]. To obtain this scaling, Nicoud and Ducros [29] proposed the WALE model based on the square of the gradient of velocity tensor:

$$\nu_{t} = L_{m}^{2} \frac{\left(\mathcal{S}_{ij} \mathcal{S}_{ij}\right)^{3/2}}{\left(\mathcal{S}_{ii} \mathcal{S}_{ii}\right)^{5/2} + \left(\overline{S}_{ii}\overline{S}_{ij}\right)^{3/2}} \tag{18}$$

where

$$L_m = \min(\kappa d_{wn}, C_w \Delta) \tag{19}$$

and

$$\mathscr{S}_{ij} = \frac{1}{2} \left( \overline{g}_{ij}^2 + \overline{g}_{ij}^2 \right) \tag{20}$$

with  $\overline{g}_{ij} = \partial \overline{u}_i/\partial x_j$ ,  $\overline{g}_{ij}^2 = \overline{g}_{ik}\overline{g}_{kj}$ , WALE model constant  $C_w = 0.325$ , and  $\Delta$ , the local grid scale, taken as the cube root of the cell volume. Nicoud and Ducros [29] show that  $\mathcal{S}_{ij}\mathcal{S}_{ij}$  may be expressed as

$$\mathscr{S}_{ij}\mathscr{S}_{ij} = \frac{1}{6} \left( S^2 S^2 + \Omega^2 \Omega^2 \right) + \frac{2}{3} S^2 \Omega^2 + 2V_{S\Omega}$$
 (21)

where

$$S^{2} = \overline{S}_{ij}\overline{S}_{ij}, \ \Omega^{2} = \overline{\Omega}_{ij}\overline{\Omega}_{ij}, \ V_{S\Omega} = \overline{S}_{ik}\overline{S}_{ik}\overline{\Omega}_{jl}\overline{\Omega}_{li}$$
 (22)

with  $\overline{\Omega}_{ij}$  the vorticity tensor defined in (13). Thus, as noted by Nicoud and Ducros [29], this model is expected to detect turbulence structures with either (large) strain rate, rotation rate or both.

## 4. Computational setup

### 4.1. Laboratory-scale simulations

#### 4.1.1. Reynolds number

LES of laboratory-scale full-depth LC with a finite volume (FV) numerical scheme at Reynolds number ( $Re_r$ ) of 395 based on wind stress friction velocity,  $u_r$ , and water column half-depth,  $\delta = H/2$  following the pseudo-spectral LES of Tejada-Martinez and Grosch [14] which were performed with this same Reynolds number. In these simulations, under statistical equilibrium, the wind stress is balanced by the mean wall shear stress, resulting in the bottom mean friction velocity ( $u_*$ ) being equal to  $u_r$ . This latter condition was approximately satisfied during the field measurements of Gargett et al. [2] and Gargett and Wells [4]. Furthermore, no temperature effects were considered, thus the buoyancy term was excluded from Eq. (2), also based on the field measurements of Gargett et al. [2].

Solving the dimensionless Navier-Stokes equations, nondimensionalized with  $u_{\tau}$  and  $\delta$ , at a specified Reynolds number, say,  $Re_{\tau}=395$ , gives rise to the non-dimensional velocity  $\overline{u}_{i}^{nd}=\overline{u}_{i}/u_{\tau}$  where  $\overline{u}_i$  is the dimensional velocity. Tejada-Martinez et al. [23] showed that the resolved non-dimensional velocity fluctuations obtained from pseudo-spectral LES at  $Re_{\tau} = 395$  dimensionalized by multiplying by the wind stress friction velocity measured in the field by Gargett et al. [2] during the presence of full-depth Langmuir cells ( $u_{\tau} = 0.01$  m/s corresponding to a wind stress of 0.1 Pascals) are in good agreement with the velocity fluctuations measured in the field. This agreement was attributed to a Reynolds number-independence of the flow which is likely because the resolved full-depth cells are efficient at mixing momentum vertically throughout the water column regardless of the value of the Reynolds number. This mixing leads to a near-zero vertical gradient of the mean downwind velocity and thus a near-zero vertical shear throughout the bulk of the water column. Thus, the dynamics of the full-depth Langmuir cells are nearly inviscid throughout the bulk of the water column regardless of the value of  $Re_{\tau}$  in the simulation. Henceforth, the computational setup will be described in both units of  $\delta$  and in scale-up dimensional units. Results will also be presented in scale-up dimensional units.

## 4.1.2. Domain and boundary conditions

The computational domain consists of a 3-D channel (see Fig. 2) with a wind sheared rigid lid surface and periodicity in the downwind ( $x_1$  or x) and crosswind ( $x_2$  or y) directions. Standard wall functions [30] were used to calculate the bottom wall shear stress based on the velocities at the first grid cell centers above the wall. Grid cell sizes are given further

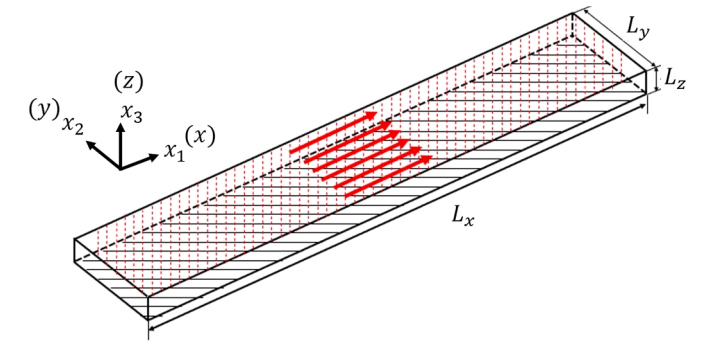


Fig. 2. Schematic of computational domain. Red arrows denote the wind stress.

below.

The channel height (along  $x_3$  or z) is H=15 m, corresponding to the depth of the water column in the coastal ocean observations of full-depth LC of Gargett et al. [2] and Gargett and Wells [4]. The downwind length of the domain is  $L_x=40\pi\delta=942.5$  m and the crosswind length is  $L_y=(16/3)\pi\delta=125.7$  m, where  $\delta=H/2=7.5$  m. Note that these lengths are greater than the lengths used in the original pseudo-spectral LES of this flow by Tejada-Martinez and Grosch [14] ( $L_x=4\pi\delta, L_y=(8/3)\pi\delta$ ) in order to allow for the full spatiotemporal development of the large scale LC (starting from rest condition), characterized by so-called y-junctions and overall length scales consistent with the field observations. The earlier simulations of Tejada-Martinez and Grosch [14] did not evolve from rest but rather from a Couette flow where the large scales of the turbulence consisted of Couette cells.

Using the domain lengths  $L_x=4\pi\delta$  and  $L_y=(8/3)\pi$   $\delta$ , the Tejada-Martinez and Grosch [14] LES captured a single LC pair with crosswind width consistent with the field measurements of Gargett et al. [2] and Gargett and Wells [4]. They also showed that a second simulation with  $L_x=4\pi\delta$  but with double the crosswind domain width  $(L_y=(16/3)\pi$   $\delta)$  yielded two LC pairs, demonstrating that the width of the LC obtained was not an artifact of the finite domain size. Thus, it is expected that the new simulations in the present study with  $L_y=(16/3)\pi$   $\delta$  should capture 2 LC pairs.

For the current study, preliminary simulations with the pseudospectral LES code of Tejada-Martinez and Grosch [14] initiated from rest led to the determination of the domain length as  $L_x=40\pi\delta$  long in the downwind direction in order to allow for the development of the expected two LC pairs of width consistent with the field measurements. Smaller values of  $L_x$  were observed to hinder this development leading to cells of smaller crosswind width. Note that this temporal evolution of full-depth LC from rest (to be further described below in the Results section) is important to represent for future studies investigating, for example, the behavior of LC under the time-varying wind and wave forcing conditions occurring in the field.

## 4.1.3. Grid resolution

In wall-resolved LES of plane channel flows (assuming a structured grid), the wall distance to the center of the cells adjacent to the wall measured in "plus" or wall units is usually taken as  $z_1^+=1$ , where wall units are defined as  $x_i^+=x_i\;u_*/\nu$ . Thus, with  $z_1^+<5$ , the grid resolves down to the Law of the Wall viscous sublayer. Furthermore, the streamwise (downwind) and spanwise (crosswind) cell sizes are taken to be in the approximate ranges of  $\Delta x^+\cong 50$ –150 and  $\Delta y^+\cong 15$ –40 [21]. In wall-modeled LES or WMLES, outer layer structures (outside of the Law of the Wall log-layer) are assumed to interact weakly with the inner layer, thus a coarser mesh is permitted resolving down only to the log-layer and thus  $z_1^+$  is set to lie within this layer. Furthermore,  $\Delta x^+\cong 100$ –600 and  $\Delta y^+\cong 100$ –300 [21].

In the present simulations, a uniform grid in the downwind, crosswind, and vertical directions was employed consisting of 300 cells along

x, 120 cells along y, and 64 cells along z, respectively. This grid is more commensurate with WMLES than wall-resolved LES. Note that the first cell center is at a distance of  $z_1^+ = 6.2$  from the wall, which is within the Law of the Wall buffer layer above the viscous sublayer. This resolution reaches below the log-layer based on the reported interaction that occurs between full-depth LC and the log-layer. Tejada-Martinez et al. [31] showed that full-depth LC can give rise to a deviation away from the log-law in the mean velocity, suggesting that the mesh should have good resolution of the log-layer region. Although the log-law deviation was also observed by Deng et al. [12,13], they found that the deviation was more pronounced at Re  $_{\tau} = 395$ , compared to Re $_{\tau} = 1000$ . However, Tejada-Martinez et al. [31] also reported that the downwelling limbs of full-depth LC impinge on the bottom boundary layer within the log layer region, thereby thinning the overall bottom boundary layer, while the upwelling limbs cause the opposite effect. Thus, within the individual limbs of the LC, the deviation away from the log law may still be significant, even at high Reynolds numbers. As such, the present LES were performed with  $z_1^+ = 6.2$  (corresponding to resolution extending below

Finally, the grid spacing in the downwind and crosswind directions is  $\Delta x_1^+ = u_r \ \Delta x_1/\nu = 165.5$  and  $\Delta x_2^+ = u_r \ \Delta x_2/\nu = 55$ , respectively, which are on the finer end of the approximate range specified for WMLES by Piomelli [21] (see further above). The potential impact of a coarser mesh on results will be discussed further below.

Results from the finite volume laboratory-scale LES with the different forms of SGS models described earlier will be compared with results obtained from the pseudo-spectral LES code of Tejada-Martinez and Grosch [14]. The pseudo-spectral LES was performed with the domain lengths specified earlier,  $L_x=40\pi\delta$ ,  $L_y=(16/3)\pi\delta$ , where  $\delta=H/2$  is the channel half-height. The number of grid cells were 320 along x, 128 along y, and 96 along z. The grid was stretched in the vertical such that the z-distance in plus units from the wall to the first grid point above the wall is  $z_1^+=1$ . The latter ensures resolution down to the viscous sublayer. The z-distance in plus units from the surface to the first grid point below the surface is also  $z_1^+=1$ .

## 4.1.4. Wind and wave forcing conditions

Simulations started from rest with sudden imposition of the wind stress (such that  $Re_{\tau} = u_{\tau}\delta/\nu = 395$ ) and the C-L vortex force. The characteristic Stokes drift velocity,  $\sigma ka^2$ , appearing in (4) and ultimately in the vortex force in (2), when non-dimensionalized by the wind stress friction velocity,  $u_{\tau}$ , gives rise to the turbulent Langmuir number, defined as  $La_t = \sqrt{u_\tau/(\sigma ka^2)}$ . The latter is representative of wave forcing relative wind forcing. A wind stress of 0.1 N m<sup>-2</sup>, a wave period of 8 s, a wavelength of 90 m and an amplitude of 0.6 m, measured during the full-depth LC field measurements of Gargett et al. [2], gives rise to  $La_t = 0.7$  (using the wave dispersion relation). Accordingly, the C-L vortex force was set to give rise to this same value of  $La_t$  in the LES ensuring that the wind forcing relative to wave forcing in the lab-scale simulations was the same as in the field. Furthermore, the wavelength in the sinh and cosh functions in (4), appearing through the wavenumber  $k = 2\pi/\lambda$  with  $\lambda$  being the wavelength, was set to  $\lambda = 6H = 12\delta$ in the simulations. This is consistent with the wavelength of 90 m and water column depth of 15 m registered in the field measurements.

## 4.2. Field-scale simulation

Field-scale LES of full-depth LC under a time varying surface heat flux was performed following field measurements of Gargett et al. [25]. These simulations were performed at the field-scale Reynolds number primarily to avoid having to scale down the surface heat flux to lab-scale. Note that non-dimensionalizing the buoyancy term in the momentum equations would bring about an additional dimensionless number in the form of a Rayleigh number (for cooling) or a Richardson number (for heating).

The LES was performed with the finite volume method with the wall-adapting S-Omega SGS model described earlier, as this model was found to provide results more consistent with pseudo-spectral LES than the other models for the simulation at  $Re_{\tau}=395$  (to be shown further below). In the field-scale simulation, the crosswind width of the domain in Fig. 2 was specified to resolve a single pair of full-depth LC (smaller than the width of the domain in the laboratory-scale simulations). The reason for the smaller width is that the aim of the field-scale LES is to investigate the effect of surface heating on the turbulence associated with existing LC, rather than on the development of LC studied via the laboratory-scale simulations. The downwind and crosswind lengths of the domain (Fig. 2) were taken as  $L_x = L_y = 62.8$  m, respectively, and the water column height as H = 15 m (the latter following the field measurements of Gargett et al. [25]).

Periodicity was enforced in the downwind and crosswind directions. Standard wall functions [32] were used to calculate the bottom wall stress based on the velocities at the first cell centers above the wall.

The simulation was initiated from rest with filtered temperature set as  $\overline{T} = T_0$  (where recall that  $T_0$  is the reference temperature in (2)), and with zero surface and bottom heat fluxes, thus no buoyancy effects. The wave parameters were set to be the same as those described in the previous Section. The wind stress was taken as 0.1 N m<sup>-2</sup> (corresponding to a wind speed of 7.8 m s<sup>-1</sup> at 10 m above the surface of the ocean) based on the measurements of Gargett [25], resulting in a wind stress friction velocity  $u_{\tau} = 0.01 \text{ m s}^{-1}$  and a friction Reynolds number  $Re_{\tau} = 75000$ . Once the simulation reached statistical equilibrium characterized by a single-pair full-depth LC and a mean bottom wall shear stress matching the wind stress, the surface heat flux was set to 205 Watts m<sup>-2</sup> (surface cooling or destabilizing) beginning the buoyancy effects. The surface heat flux was subsequently dropped in a stepwise fashion to -600 Watts m<sup>-2</sup> (surface heating or stabilizing) over a period of 10 h to investigate the decay of the turbulence, following the measurements of Gargett [25]. Throughout this time, the wind and wave forcing remained constant. Further details of the stepwise variation of the surface heat flux will be given when describing the results.

A uniform grid was used in the downwind and crosswind directions with 256 elements in both directions. In the vertical direction, 96 stretched elements were used. The element length in both the downwind and crosswind directions is 0.25 m. The element length in the vertical is 0.05 m at the wall and at the surface and 0.22 m at mid-depth. These element sizes are comparable to those in the pseudo-spectral field-scale LES of Kukulka et al. [9], who performed simulations of LC under a wind speed of 5 m s<sup>-1</sup> in a water column 20 m in height. Furthermore, in the present mesh, the first cell center above the wall is at a distance 0.025 m away from the wall, well within the log-layer limit suggested by Pope [26],  $z^+ > 30$  and  $z < 0.3\delta$ . For the present case with  $\delta = 7.5$  m,  $z < 0.3\delta = 2.25$  m.

## 4.3. Numerical methods

For both laboratory-scale and field-scale simulations described above, the governing continuity, momentum and temperature equations described earlier were solved using the finite volume method. The solution algorithm involved the simultaneous solution of the momentum equation and the pressure equation form of the continuity equation [33] on a staggered grid [34]. The method employs a bounded central difference (BCD) scheme [35] for advection, least-squares gradient reconstruction [36], and implicit second order accurate time stepping via the approximation of the time derivative of scalar  $\phi$  at time level  $t_{n+1}$  as

$$\dot{\phi}^{n+1} = \frac{3\phi^{n+1} - 4\phi^n + \phi^{n-1}}{2\Delta t} \tag{23}$$

The time step  $\Delta t$  was chosen such that the Courant-Friedrichs-Lewy (CFL) number was approximately 1.

The BCD scheme is equipped with a detector for identifying oscillations in wavelengths that are  $2\Delta x$  or shorter. In situations where such oscillations are detected, the scheme reverts to a second-order upwind scheme, or, in the worst case, to a first-order upwind scheme. More information about this approach is given by Leonard [35], Moukalled et al. [36] and Ask and Davidson [37]. Ask and Davidson [37] have shown that the BCD scheme described above is less dissipative than second-order upwinding in simulations of the air flow around a generic side mirror of a car. Overall, the BCD scheme provides minimal numerical dissipation within the family of stable advection discretization schemes in the finite volume framework.

As the numerical methods employed here are standard throughout the computational fluid dynamics community, the ANSYS Fluent platform [17] was used to carry out the simulations.

## 4.4. Performance of SGS models in shear turbulence

Prior to presenting results of the simulations with LC, the performance of the finite volume LES with the various SGS models described earlier is evaluated for the wind-driven (surface shear-driven) flow at  $Re_{\tau} = 395$  described above in Section 4a but without C-L vortex forcing (i.e. without LC) on the corresponding finite volume mesh also described above. Results obtained from these simulations under statistical equilibrium shown in Fig. 3 in terms of mean downwind velocity and resolved velocity variances do not show significant differences. Results are also shown of the pseudo-spectral LES with C-L vortex forcing for comparison, highlighting the significant variations induced by the LC. As such, it is important to understand how well LES with the different SGS models can capture these variations and the overall Langmuir cell structure. As noted in the introduction, Tejada-Martinez and Grosch [14] reported that the full-depth Langmuir cells contribute between 50 and 80 % of the TKE throughout the water column. Thus, it should be expected that inaccuracies in the representation of the full-depth cell structure will be reflected in the depth-profiles of the velocity variances as will be shown in the next section.

### 5. Results

## 5.1. Laboratory-scale simulations

## 5.1.1. Cell development and structure: S-Omega SGS model

The development of the Langmuir cells from rest in the finite volume LES with the wall-adapting S-Omega model can be seen in Fig. 4 in terms of downwind-averaged vertical velocity fluctuations. The cells are initially regular or smooth. As time progresses, the cells become unstable and undergo a merging or amalgamation process in which they grow in width (along the crosswind direction) and depth while becoming more irregular as the flow transitions to Langmuir turbulence. After about 1 h, the cells reach close to the bottom, which can be seen in terms of the full-depth downwelling and upwelling limbs, or full-depth regions of negative and positive vertical velocity fluctuations, respectively. After approximately 30 h, the largest scales of the turbulence, corresponding to the full-depth LC, have stopped growing with the computational domain able to capture two pairs of cells, as expected and described earlier.

The overall cell structure in equilibrium obtained in the LES with the wall-adapting S-Omega model is shown in Fig. 5, in terms of downwind-averaged crosswind, vertical and downwind velocity fluctuations at  $t=30\,\mathrm{h}$ . in panels (a)–(c) respectively. Equilibrium refers to the fact that the cells have reached a stable length scale and thus are no longer merging. The surface convergences and bottom divergences and the full-depth downwelling and upwelling limbs of the LCs resolved in the LES can be seen in panels (a) and (b) of Fig. 5, respectively, highlighted by the white arrows. Note that the surface convergences of the cells lead to the downwelling limbs, and the bottom convergences lead to the upwelling limbs. Furthermore, the downwelling limbs coincide with full-depth

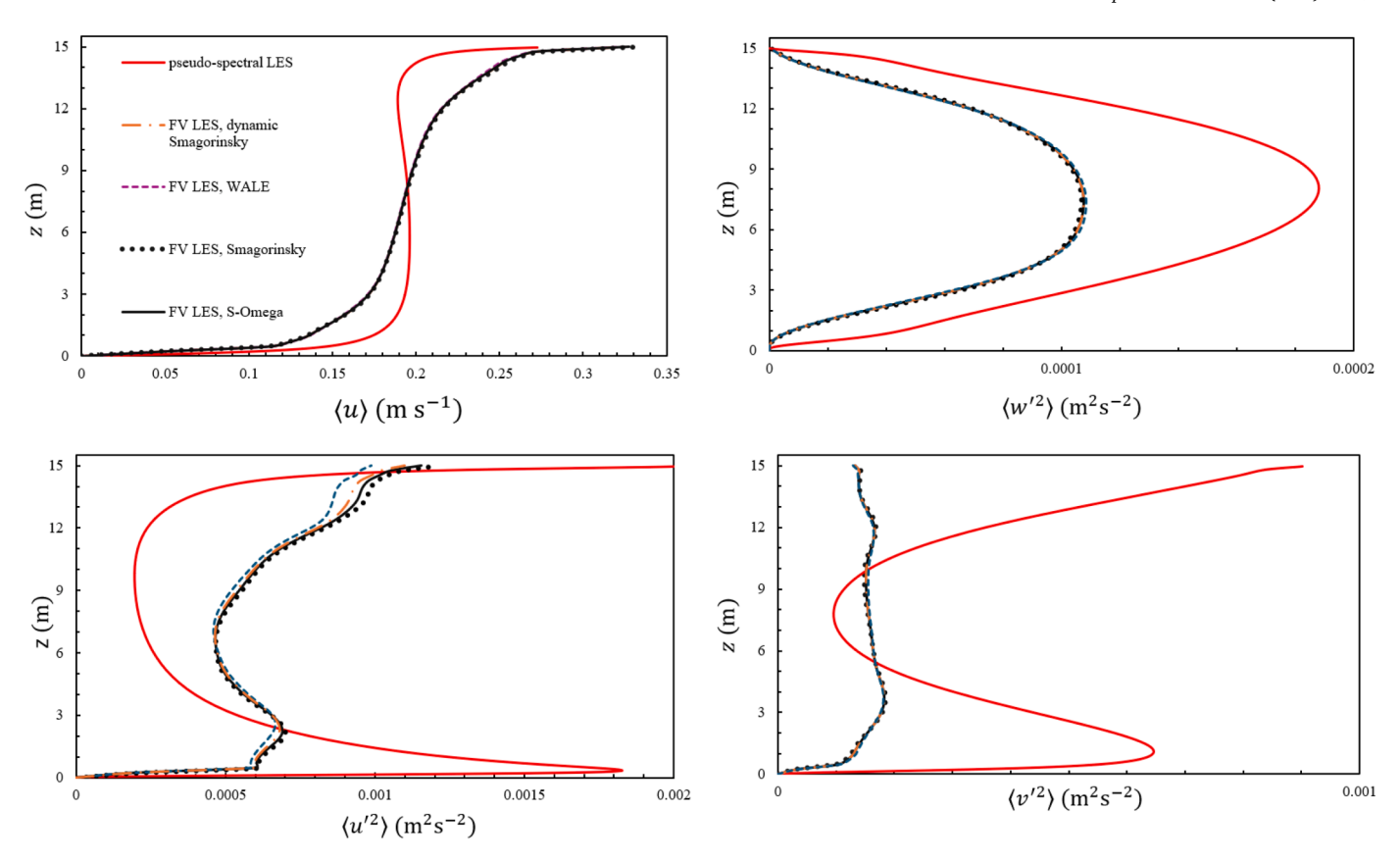


Fig. 3. (a) Mean downwind velocity and (b) vertical (c) downwind and (d) crosswind velocity variances in finite volume (FV) LES of wind-driven flow without LC. Mean downwind velocity and velocity variances obtained in pseudo-spectral LES with LC are shown (in red) for reference. Brackets denote averaging over time and over the downwind and crosswind directions.

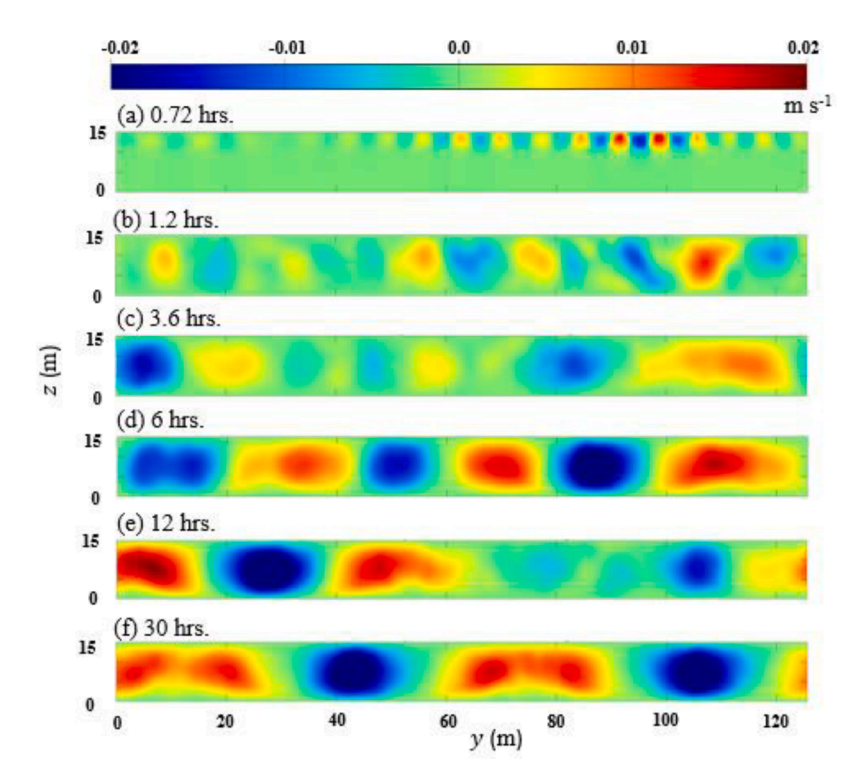
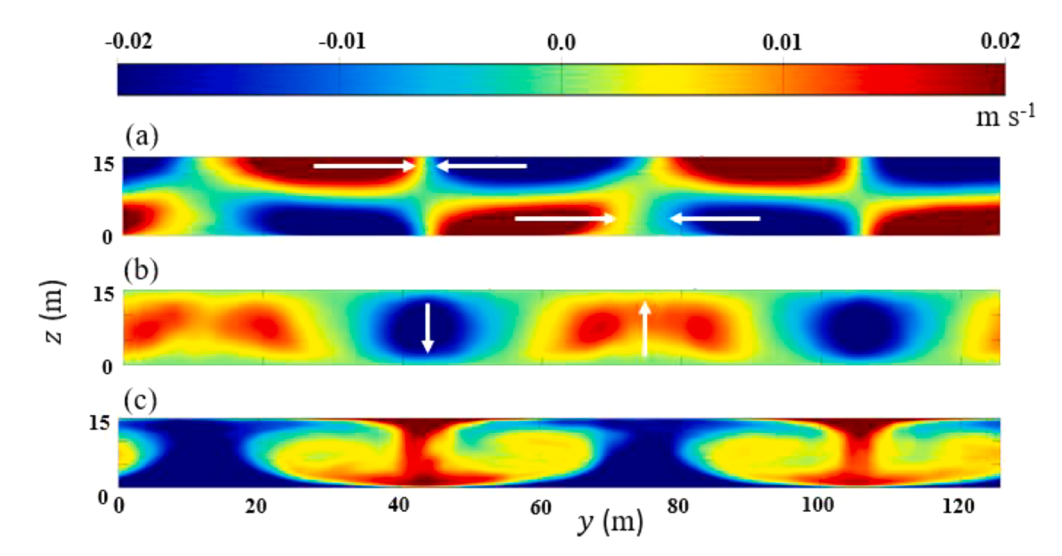


Fig. 4. Instantaneous downwind averaged vertical velocity fluctuations over the vertical (z) and crosswind extents (y) of the computational domain in finite volume LES with the S-Omega SGS model.



**Fig. 5.** Instantaneous downwind-averaged crosswind (a), vertical (b), and downwind (c) velocity fluctuations over the vertical (z) and crosswind extents (y) of the computational domain at t = 30 h. in finite volume LES with the S-Omega SGS model.

regions of positive downwind velocity fluctuations, which are intensified near the surface and near the bottom (Fig. 5c). Such bottom intensification of downwind velocity fluctuations has been observed in the field during episodes of full-depth LC by Gargett and Wells [4] and is considered a key signature of full-depth LC distinguishing it from the LC traditionally observed in the upper ocean mixed layer (e.g. see [1]). The coincidence of the downwelling limbs with full-depth regions of positive downwind velocity fluctuations is because the downwelling limbs entrain fluid possessing fast downwind velocity from the surface into the water column, reaching close to the bottom. Analogously, the upwelling limbs of the cells transport fluid possessing slow downwind velocity from the bottom towards the surface.

## 5.1.2. Cell structure: comparison between all SGS models

The development of the cells over time can be further explored in terms of the instantaneous vertical velocity fluctuations over the horizontal plane (i.e., the *x-y* plane) at mid-depth. On this plane, the vertical velocity fluctuations are characterized by positive and negative streaks

corresponding to the upwelling and downwelling limbs of the LC, respectively. Fig. 6 shows these streaks at 12 h and 30 h after the finite volume LES simulations with the different SGS stress models were initiated from rest. The corresponding results obtained with the pseudospectral LES code of Tejada-Martinez and Grosch [14] are also shown in Fig. 6. As observed earlier in Fig. 5, with time, the cells grow in depth and width. This is reflected in Fig. 6 through the meandering and merging of streaks, forming so-called "y-junctions", often used to describe the manifestations of LC on the surface of lakes, rivers, bays, and oceans (e.g., see Thorpe [38] and photograph of windrows in Fig. 1). At t = 12 h., the pseudo-spectral LES solution reveals three pairs of streaks, with two of the positive streaks in the process of merging (Fig. 6k). Similar y-junctioning may be observed in the finite volume LES with the wall-adapting S-Omega SGS model (Fig. 6g). By t = 30 h., when the cells have stopped growing and reached equilibrium, both simulations reveal two pairs of streaks (Fig. 6, panels h and l). Although a similar behavior is seen in the finite volume LES with the other SGS stress models (the WALE, dynamic Smagorinsky and wall-adapting

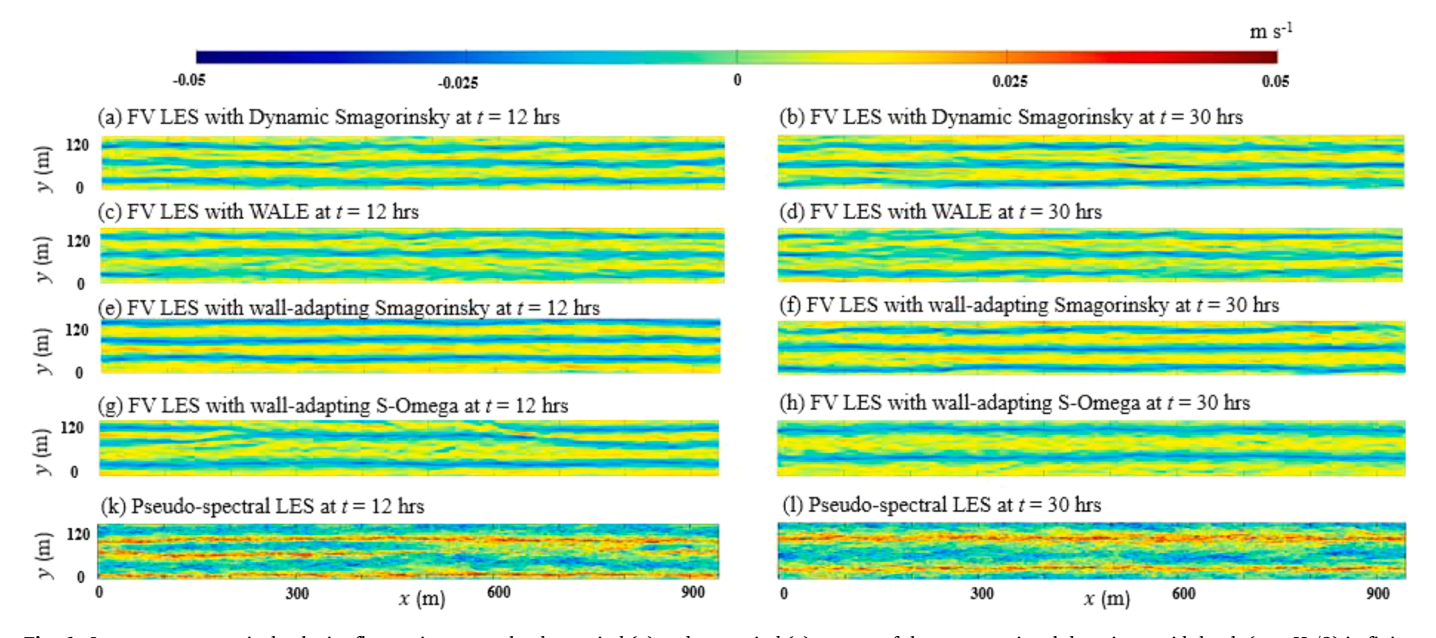


Fig. 6. Instantaneous vertical velocity fluctuations over the downwind (x) and crosswind (y) extents of the computational domain at mid-depth (z = H/2) in finite volume (FV) LES and pseudo-spectral LES.

Smagorinsky models), these solutions at  $t=30\,\mathrm{h}$ . under equilibrium are characterized by three pairs of cells (rather than two pairs). As a result, the finite volume LES with the wall-adapting S-Omega model and the pseudo-spectral LES lead to cells with greater width than the finite volume LES with the other SGS models. Note that the cells of smaller width obtained with the WALE, wall-adapting Smagorinsky and dynamic Smagorinsky models reach equilibrium before  $t=12\,\mathrm{h}$ ., which is much earlier than the cells obtained with the wall-adapting S-Omega model and the pseudo-spectral LES.

The equilibrium cell structure obtained with the finite volume LES with the different SGS models, and the pseudo-spectral LES is shown in Figs. 7–9 in terms of downwind-averaged crosswind, vertical, and downwind velocity fluctuations, respectively, at  $t=30\,\mathrm{h}$ . The two cell pairs obtained with the pseudo-spectral LES and the finite volume LES with the S-Omega model and the three cell pairs obtained with the finite volume LES with the other SGS models can again be appreciated in these figures.

The pseudo-spectral LES and the finite volume LES with the S-Omega SGS model lead to cells for which the maximum downwelling velocities are stronger than the upwelling velocities, with the downwelling limbs being narrower than the upwelling limbs in order to satisfy mass conservation (Fig. 8, panels (d) and (e)). This asymmetry between the upwelling and downwelling limbs of the cells is consistent with the field measurements of LC of Gargett and Wells [4]. Furthermore, this asymmetry is not as pronounced in the cells obtained with the finite volume LES with the wall-adapting Smagorinsky, the dynamic Smagorinsky, and the WALE models (Fig. 8, panels (a)–(c)).

Another important feature of the cells obtained with the pseudo-spectral LES and the finite volume LES with the wall-adapting S-Omega model is that the cells' downwell-to-downwell width is approximately 60 m (Fig. 8, panels (d) and (e)), corresponding to  $\sim 4H$  (H=15 m), consistent with the range 3H-6H reported by Gargett and Wells [4] in their observations of full-depth LC over periods greater than 20 h. The width of the cells obtained in the finite volume LES simulations

with the WALE, dynamic Smagorinsky and wall-adapting Smagorinsky models is less at  $\sim 3H$  (Fig. 8, panels (a), (b), and (c)).

The only difference between the wall-adapting Smagorinsky and S-Omega models in Eqs. (10) and (12), respectively, is in the velocity scale. Thus, it may be concluded that the S-Omega model's velocity scale given through  ${\rm abs}(|\overline{S}|-|\overline{\Omega}|)$  is an important factor enabling the resolved full-depth LC in finite volume LES to possess a morphology or structure in better agreement with the LC in pseudo-spectral LES and the field observations of Gargett and Wells [4]. This would be expected as the velocity scale based on  ${\rm abs}(|\overline{S}|-|\overline{\Omega}|)$  should be able to reflect the importance of rotation in LC flows better than the velocity scale based solely on  $|\overline{S}|$ .

The LES with the S-Omega model and the pseudo-spectral LES lead to cells that have similar forms at the surface and at the bottom of the water column (e.g., see sketches and crosswind velocity fluctuations in Fig. 7, panels (d) and (e)). In contrast, the finite volume LES with the dynamic Smagorinsky model leads to significant differences between the nearbottom and near-surface cell structure (e.g., see sketches and crosswind velocity fluctuations in Fig. 7, panel (a)). In Fig. 7a, the crosswind velocity fluctuations reveal that the bottom convergences of the cells obtained with the finite volume LES with the dynamic Smagorinsky model are unable to fully extend across the bottom. Instead, the bottom convergences of the cells are "snipped". The weaker bottom convergences of the snipped cells are also reflected through their upwelling limbs, seen in Fig. 8a. For example, the intensity of the upwelling limbs is significantly weaker at the bottom of the water column in the LES with the dynamic Smagorinsky model (Fig. 8a) than in the LES with the S-Omega model and the pseudo-spectral LES (Fig. 8, panels (d) and (e)). Overall, a weaker intensity of the bottom convergences of the cells in the finite volume LES with the dynamic Smagorinsky model leads to weaker transport of slow downwind moving fluid from the bottom of the water column towards the surface by the upwelling limbs. This can be seen in Fig. 9a, where the regions of negative downwind velocity fluctuations in

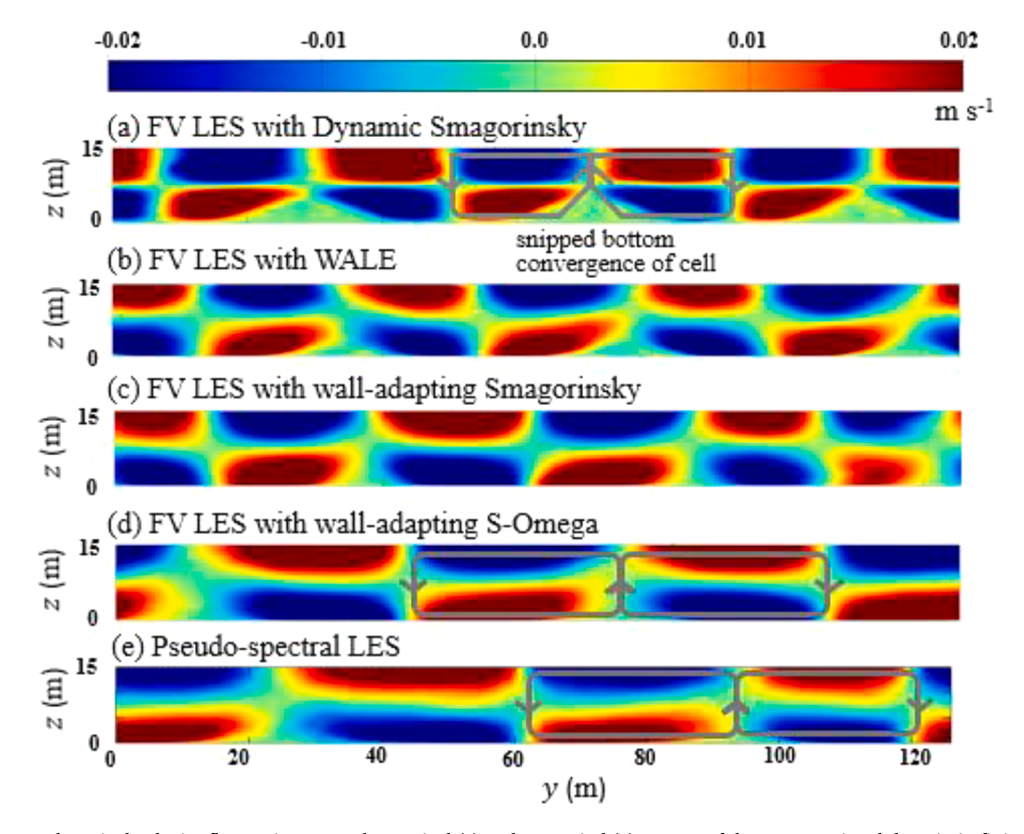


**Fig. 7.** Downwind averaged vertical velocity fluctuations over the vertical (z) and crosswind (y) extents of the computational domain in finite volume (FV) LES and pseudo-spectral LES at t = 0 h.

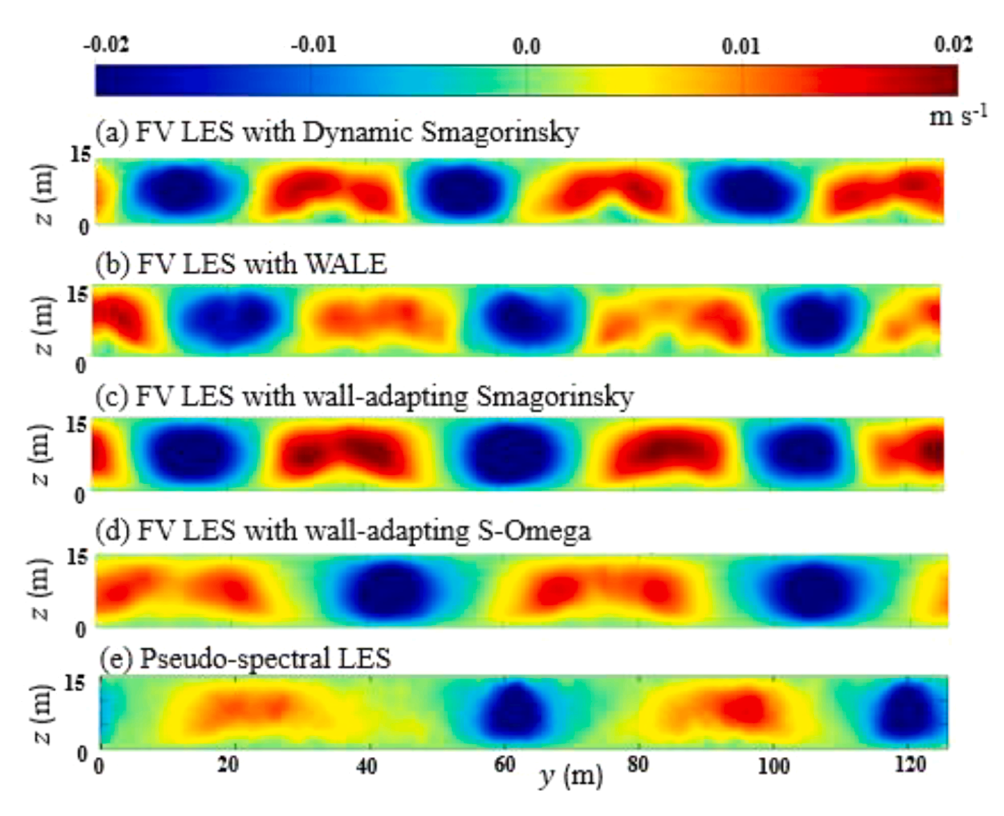


**Fig. 8.** Downwind-averaged vertical velocity fluctuations over the vertical (z) and crosswind extents (y) of the computational domain in finite volume (FV) LES and pseudo-spectral LES at t = 30 h.

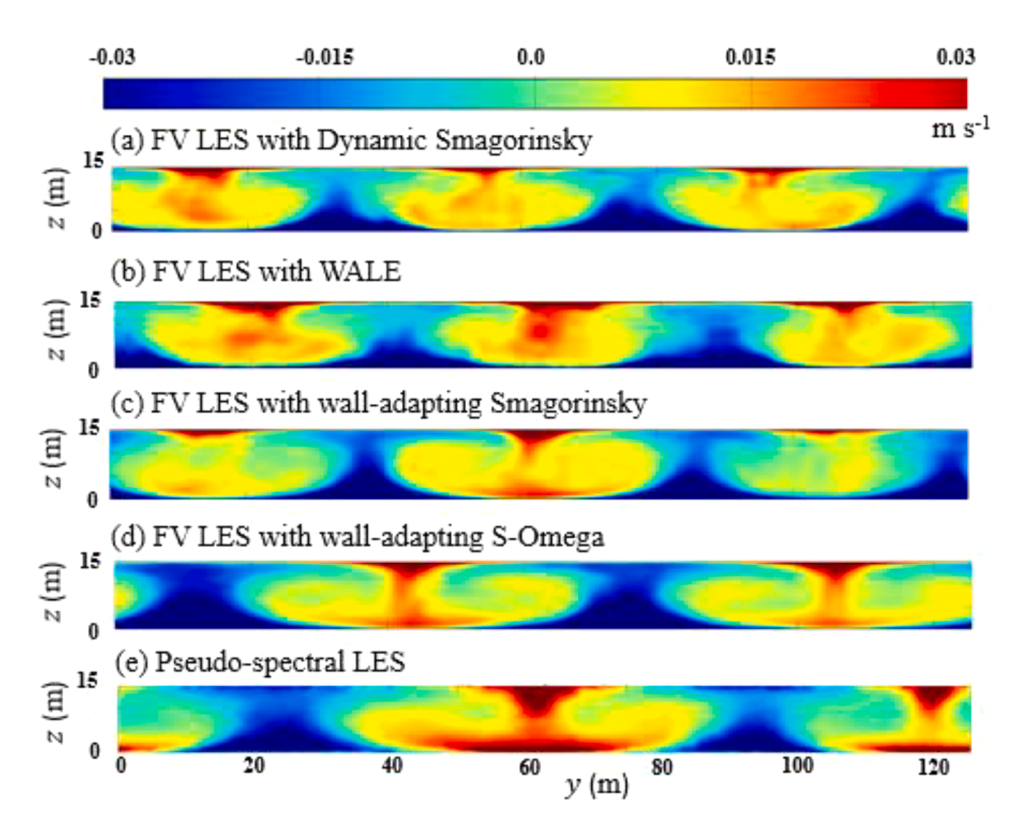


Fig. 9. Downwind averaged downwind velocity fluctuations over the vertical (z) and crosswind (y) extents of the computational domain in finite volume (FV) LES and pseudo-spectral LES at t = 30 h.

the finite volume LES with the dynamic Smagorinsky model are not as prominent near the surface compared to the same regions in the LES with the S-Omega model and in the pseudo-spectral LES (Fig. 9, panels (d) and (e), respectively).

To further quantify the impact of the SGS models on the transport of slow-moving fluid from the bottom of the water column towards the surface induced by the upwelling limbs of the full-depth Langmuir cells, Fig. 10 plots the downwind-averaged downwind velocity fluctuations over the crosswind extent of the computational domain at a depth close to the surface. As can be seen in this figure, the negative downwind velocity fluctuations reach to about  $-0.3~{\rm m~s^{-1}}$  in the finite volume LES with the S-Omega model, in good agreement with the pseudo-spectral LES. However, in the finite volume LES with the dynamic Smagorinsky model and WALE models, the negative downwind velocity fluctuations only reach to  $\sim -0.1~{\rm m~s^{-1}}$ .

# 5.1.3. Velocity statistics and cell structure: comparison between all SGS models

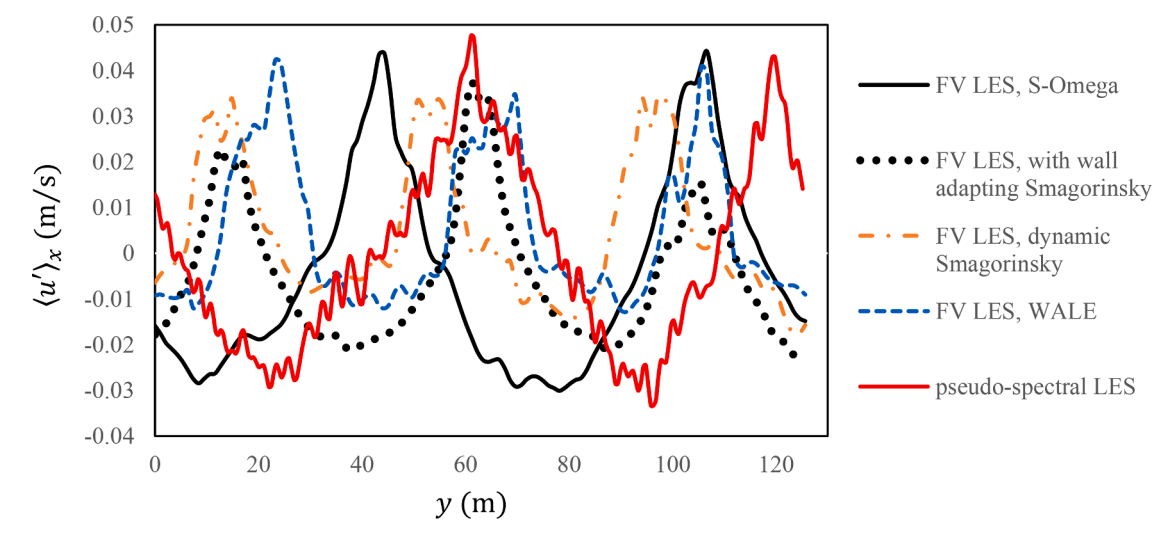
Differences can be seen across the LES with the different SGS models in terms of resolved mean downwind velocity (Fig. 11) and resolved velocity variances (Figs. 12-14). Given the well-mixed downwind velocity profiles obtained in the simulations (Fig. 11a), the characteristic bulk downwind velocity may be taken as the mean downwind velocity at mid-depth. In Fig. 11a, it can be seen that the finite volume LES with the wall-adapting S-Omega and Smagorinsky SGS models lead to slower bulk downwind velocity relative to LES with the other SGS models and relative to the pseudo-spectral LES. This may be attributed to the stronger negative downwind velocity fluctuations induced by the LC in the LES with the wall-adapting S-Omega and Smagorinsky models compared to the dynamic Smagorinsky and WALE models, as observed in Figs. 9 and 10. This may interpreted as the LC obtained with the walladapting S-Omega and Smagorinsky models serving to provide a greater resistance to the bulk flow. The slower bulk flow obtained within the wall-adapting S-Omega and Smagorinsky models could also be tied to the greater resistance from the higher near-wall eddy viscosities obtained with these models (Fig. 15).

Fig. 11b reveals that the faster bulk downwind velocity obtained with the dynamic Smagorinsky and WALE models leads to a greater deviation from the log-law in the lower half of the channel (for example at  $z^+{\sim}90)$  compared to the wall-adapting S-Omega and Smagorinsky SGS models and the pseudo-spectral LES. This bottom log-layer deviation is expected in flows with full-depth LC as discussed earlier when presenting the computational setup in Section 4a.

The differences in intensity and structure of the full-depth LC resolved in the various simulations described earlier can also be observed in terms of depth profiles of the resolved vertical, downwind, and crosswind velocity variances, under statistical equilibrium. Focus is placed on the variances in the middle and lower half of the water column rather than on the surface given that in the ocean the near-surface turbulence is strongly affected by wave-breaking and none of the simulations performed accounts for surface wave breaking.

Fig. 12 reveals that the finite volume LES with the S-Omega SGS model leads to better agreement with pseudo-spectral LES in terms of vertical velocity variance, compared to the other SGS models, in the middle of the water column. Furthermore, the vertical velocity variances obtained in the LES with the S-Omega SGS model and the pseudospectral LES are lower than in the LES with the other SGS models. This trend can be directly linked to the similar LC cell structure obtained with the LES with the S-Omega SGS and the pseudo-spectral LES. In Fig. 8 two key characteristics can be observed: (1) The finite volume LES with the S-Omega SGS model and the pseudo-spectral LES lead to cells for which the maximum downwelling velocities are stronger than the upwelling velocities, with the downwelling limbs being narrower than the upwelling limbs, as noted earlier. Meanwhile the finite volume LES with the other SGS models give rise to downwelling and upwelling velocities nearly equal in magnitude, and thus dowelling and upwelling limbs of nearly equal width. (2) The maximum downwelling velocities across all simulations are nearly the same ( $\sim -0.02 \, \mathrm{m \, s^{-1}}$ ) as well as the width of the downwelling limbs. Thus, the lower vertical velocity variances obtained in the LES with the S-Omega SGS model and the pseudospectral LES may be attributed to the wider crosswind coverage of the slower upwelling limbs in these simulations compared to the simulations with the other SGS models.

In Fig. 13, it can be seen that the finite volume LES with the WALE and the dynamic Smagorinsky models lead to near-bottom downwind velocity fluctuations that are excessively high, relative to the pseudospectral LES and the finite volume LES with either the wall-adapting S-Omega or the wall-adapting Smagorinsky models. This behavior is attributed to the lower values of the eddy viscosities obtained in the finite volume LES simulations with the WALE and the dynamic Smagorinsky models compared to the wall-adapting S-Omega and Smagorinsky models (see Fig. 15). Near the wall, the wall-adapting S-Omega and Smagorinsky models give rise to larger eddy viscosities, consistent with the hybrid Reynolds-averaged Navier-Stokes (RANS)-LES concept in which the outer layer is computed via LES and the near-wall region is treated in a Reynolds-average sense where the SGS stress should behave



**Fig. 10.** Downwind-averaged downwind velocity fluctuations vs. crosswind extent of the at domain (y) at z = 14.65 m at t = 30 h. averaged over downwind and crosswind extents of the domain in finite volume (FV) LES and pseudo-spectral LES. Note that y-regions of negative downwind velocity fluctuations correspond the upwelling limbs of the full-depth Langmuir cells and regions of positive downwind velocity fluctuations correspond to the downwelling of the cells.

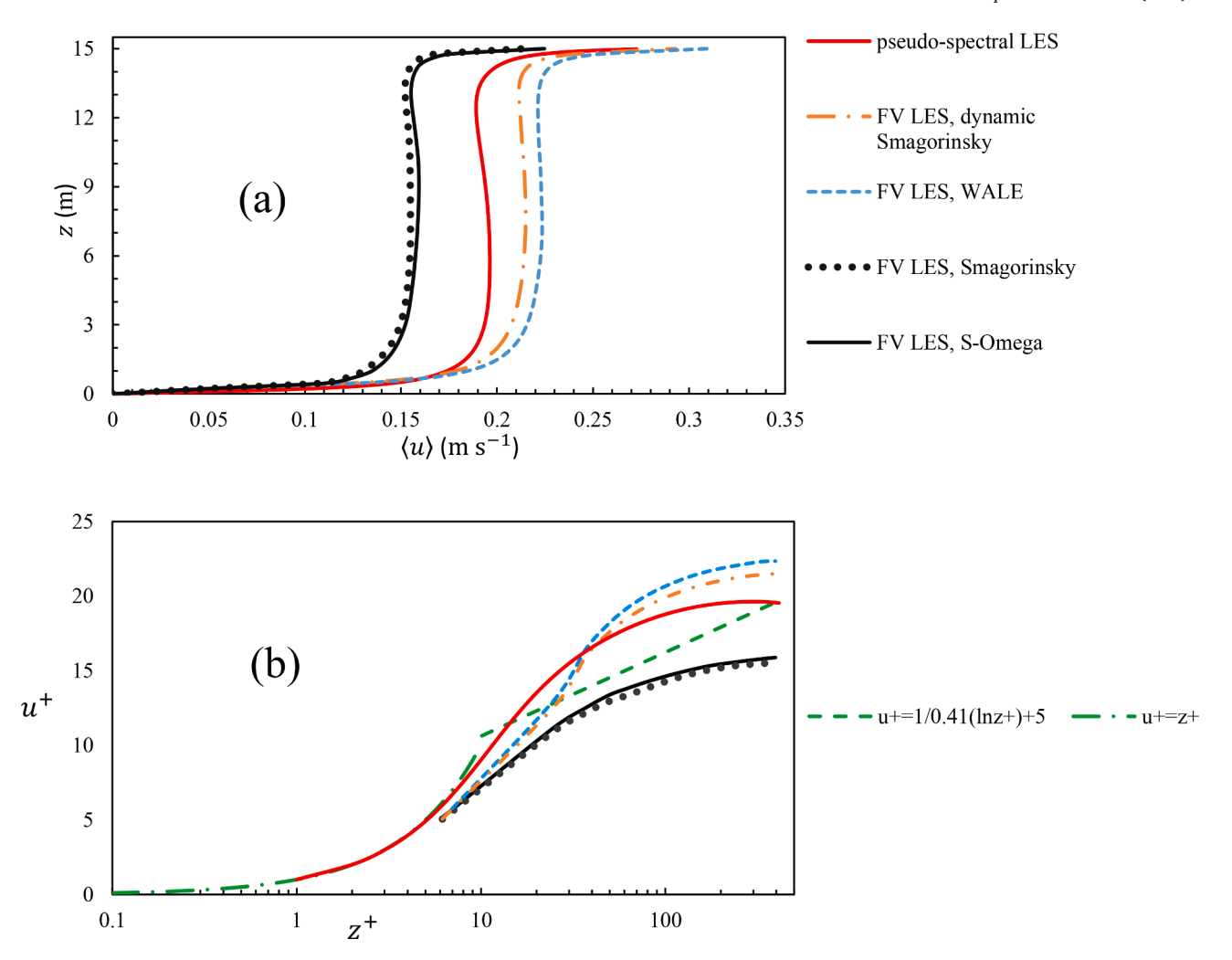


Fig. 11. (a) Mean downwind velocity profiles over the depth of the water column and (b) mean downwind velocity profiles in wall units in the lower half of the water column in finite volume (FV) LES and pseudo-spectral LES. In (b), velocity profiles based on the Law of the Wall are shown in green. Brackets denote averaging over time and over the downwind and crosswind directions.

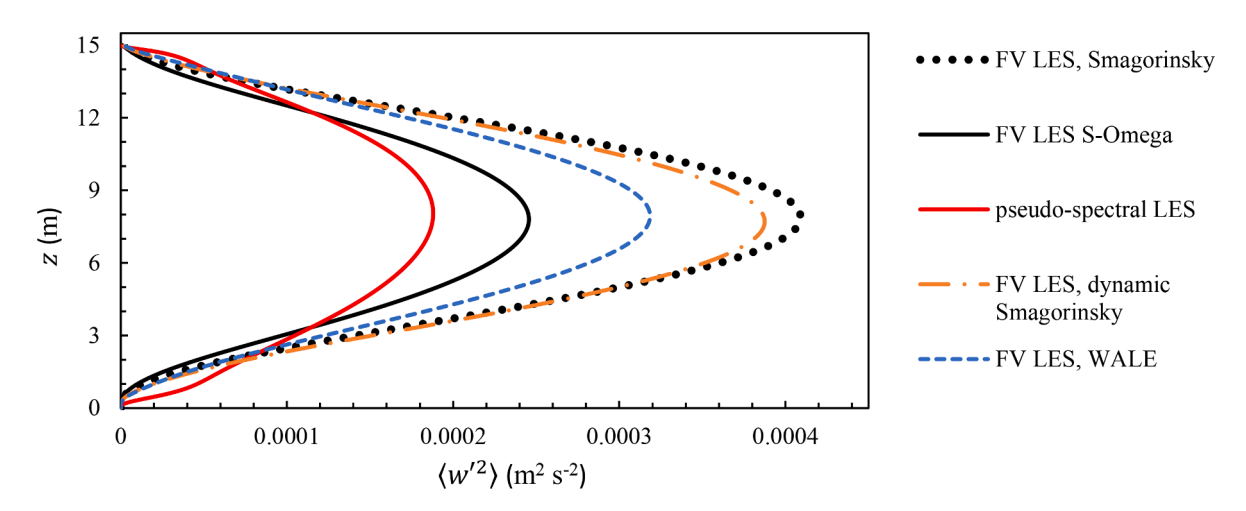


Fig. 12. Resolved vertical velocity variance in finite volume (FV) LES and pseudo-spectral LES. Brackets denote averaging over time and over the downwind and crosswind directions.

closer to classical Reynolds stress models.

The excessive near-bottom downwind velocity variances obtained with the WALE and the dynamic Smagorinsky models (relative to pseudo-spectral LES) are indicative of the over-prediction of the bottom-

generated shear turbulence resolved in the LES with these models. As a result, the bottom convergence zones of the cells and their corresponding bottom upwelling limbs obtained with these models are less prominent, compared to the cells obtained with the wall-adapting S-

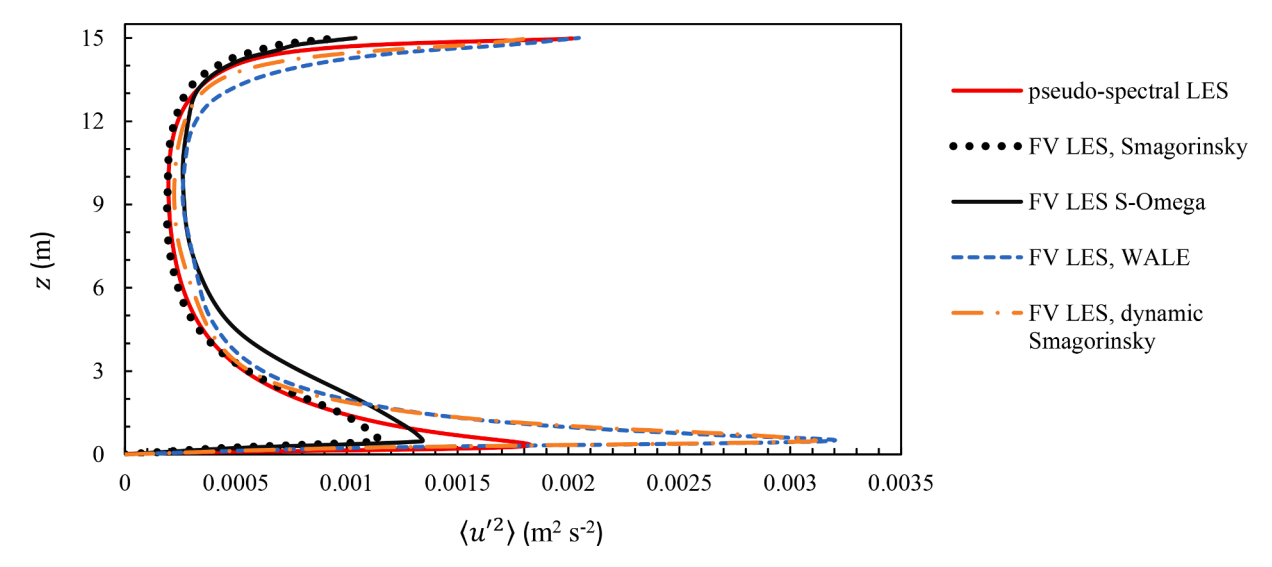


Fig. 13. Resolved downwind velocity variance in finite volume (FV) LES and pseudo-spectral LES. Brackets denote averaging over time and over the downwind and crosswind directions.

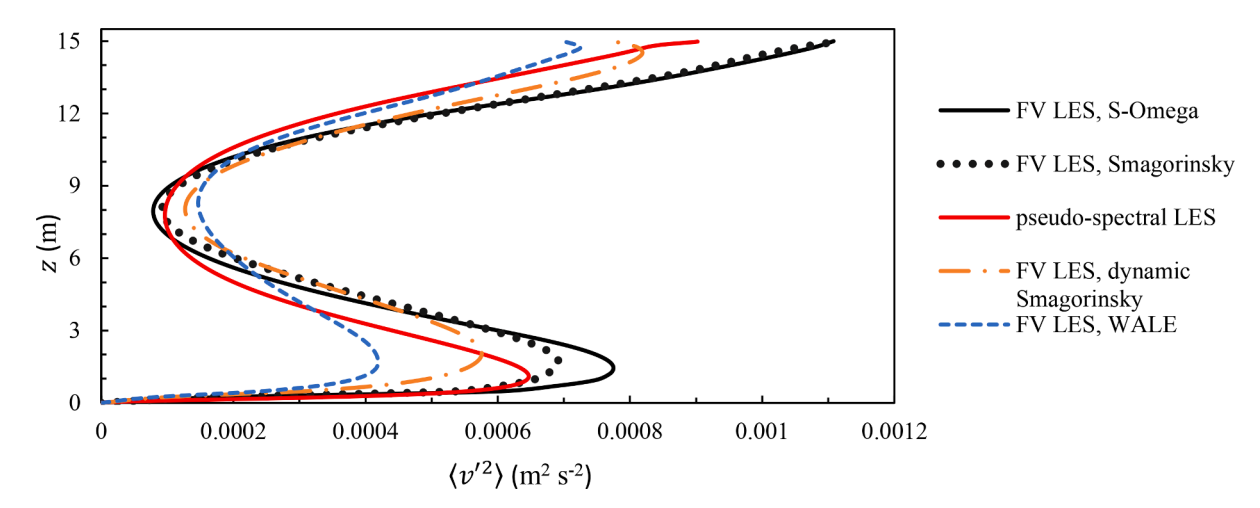


Fig. 14. Resolved crosswind velocity variance in finite volume (FV) LES and pseudo-spectral LES. Brackets denote averaging over time and over the downwind and crosswind directions.

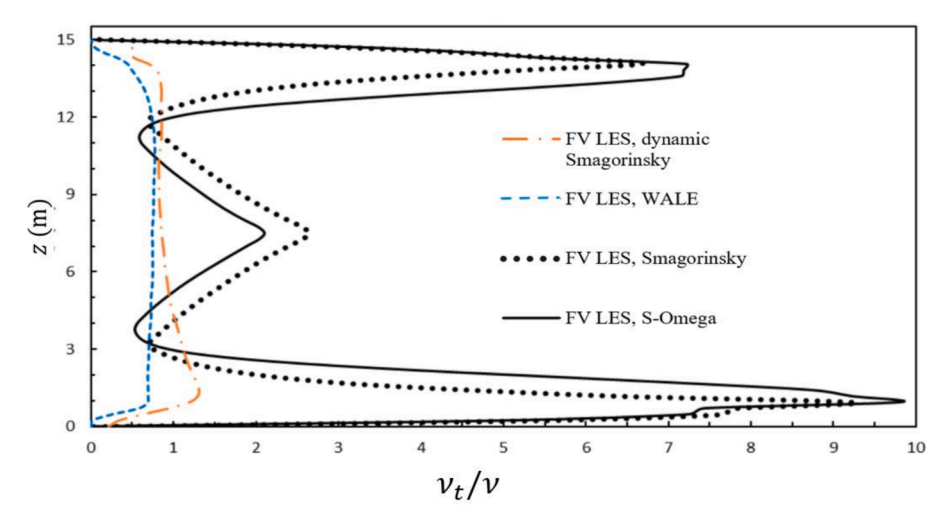


Fig. 15. Eddy viscosity scaled by molecular kinematic viscosity at t = 30 h. averaged over downwind and crosswind extents of the domain in finite volume (FV) LES.

Omega and Smagorinsky model (Figs. 7 and 8). In other words, the excessive bottom-generated shear turbulence in the LES with the WALE and dynamic Smagorinsky models may be viewed as causing disruption of the bottom development of the cells. Accordingly, the near-bottom crosswind velocity variances obtained with the WALE and dynamic Smagorinsky models are also weaker, as seen in Fig. 13.

The excessive bottom-generated shear turbulence in the LES with the WALE and dynamic Smagorinsky models can also be seen in terms of color contours of resolved turbulent kinetic energy (TKE) in Fig. 16, panels (a) and (b). In contrast, the higher near-bottom eddy viscosities provided by the wall-adapting S-Omega and Smagorinsky models (seen in Fig. 15) lead to lower levels of bottom-generated shear turbulence (i. e. lower resolved TKE in Fig. 16, panels (c) and (d)) allowing for a fuller development of the bottom convergences of the LC, relative to the cells obtained with the WALE and dynamic Smagorinsky models (see sketches in panels (a) and (d) of Fig. 16). This suggests that the high intensity of the bottom shear turbulence obtained with the WALE and dynamic Smagorinsky models prevents the bottom convergence of the cells from extending fully across the bottom, ultimately serving to disrupt or "snip" the bottom of the cells, as described earlier and shown in the sketches in Figs. 7a and 16a.

The over-prediction of bottom-generated shear turbulence with the WALE and the dynamic Smagorinsky models occurred despite the first grid cell center being within the buffer sublayer, as described in Section 4a. A coarser resolution in the wall-normal direction, more commensurate with WMLES, is likely to lead to a greater over-prediction of the bottom turbulence, and thus a poorer representation of the near-bottom LC structure.

#### 5.2. Field-scale simulations

Given the better performance of the LES with the S-Omega model compared to the other SGS models tested relative to pseudo-spectral LES, LES with the S-Omega model was subsequently tested on a case previously untried.

Gargett [25] focused on the effect of surface buoyancy on full-depth LC during the diurnal cycle. Fig. 17, borrowed from Gargett [25], shows records of depth-averaged vertical velocity variance during a period

when the surface heat flux, Q, was increasingly stabilizing during field measurements of full-depth LC. The color of each dot in Fig. 17 corresponds to the depth-averaged vertical velocity variance averaged over a two-hour period. The arrows in Fig. 17 connect dots over consecutive averaging periods. As can be seen from this figure, a period of 8 h over which the surface heat flux decreased from approximately 200 Watts m<sup>-2</sup> (destabilizing) to approximately - 400 Watts m<sup>-2</sup> (stabilizing) did not significantly affect the average vertical velocity variance, remaining at approximately 2.5 cm<sup>2</sup> s<sup>-2</sup>. A significant change was eventually observed over the last 2 h of record when the surface heat flux further decreased from  $\sim -400$  to -600 Watts m<sup>-2</sup> accompanied by a vertical velocity variance decrease of a factor of about 4.5 to 0.56 cm<sup>2</sup> s<sup>-2</sup>. In summary, a period of continuously stabilizing surface heat flux of  ${\sim}8$  h over which the surface heat flux decreased from  $\sim 200$  to  $\sim -400$  Watts m<sup>-2</sup> did not lead to significant decrease in vertical velocity variance. A delayed response was finally observed in the vertical velocity variance over hours 9 and 10 of continuous stabilizing heat flux as Q dropped from  $\sim$  $-400 \text{ to } -600 \text{ Watts m}^{-2}$ .

Field-scale LES of full-depth LC with the S-Omega model with surface buoyancy (heat) flux guided by Gargett [25] measurements was performed. The LES was initiated from rest with the wind and wave forcing described earlier in Section 4b and with zero surface heat flux until the mean bottom stress matched the surface stress. An instantaneous solution is shown in Fig. 18 in terms of the cell structure. As expected from the domain chosen (see discussion in Section 4b), one full-depth LC pair is resolved. At this point a surface heat flux of Q = 205 Watts m<sup>-2</sup> was applied, and the simulation was continued running for two hours of flow time. This time span of the simulation is denoted as 00. At the end of time span 00, the surface heat flux was switched to Q = 200 Watts m<sup>-2</sup> and the simulation was continued for another two hours of flow time. This latter time span is denoted as 01. Similar two-hour flow simulation time spans were continued for which the surface heat flux was changed to Q = 0, Q = -400 Watts m<sup>-2</sup>, and Q = -600 Watts m<sup>-2</sup> at the end of each time span. These simulation time spans are denoted as 02, 03, 04, respectively in Fig. 19. Results are shown in Fig. 19 and Table 1 in terms of resolved vertical velocity variance averaged over the downwind and spanwise directions and averaged over the last 15 min of each time span. The vertical velocity variances reported in Table 1 were further

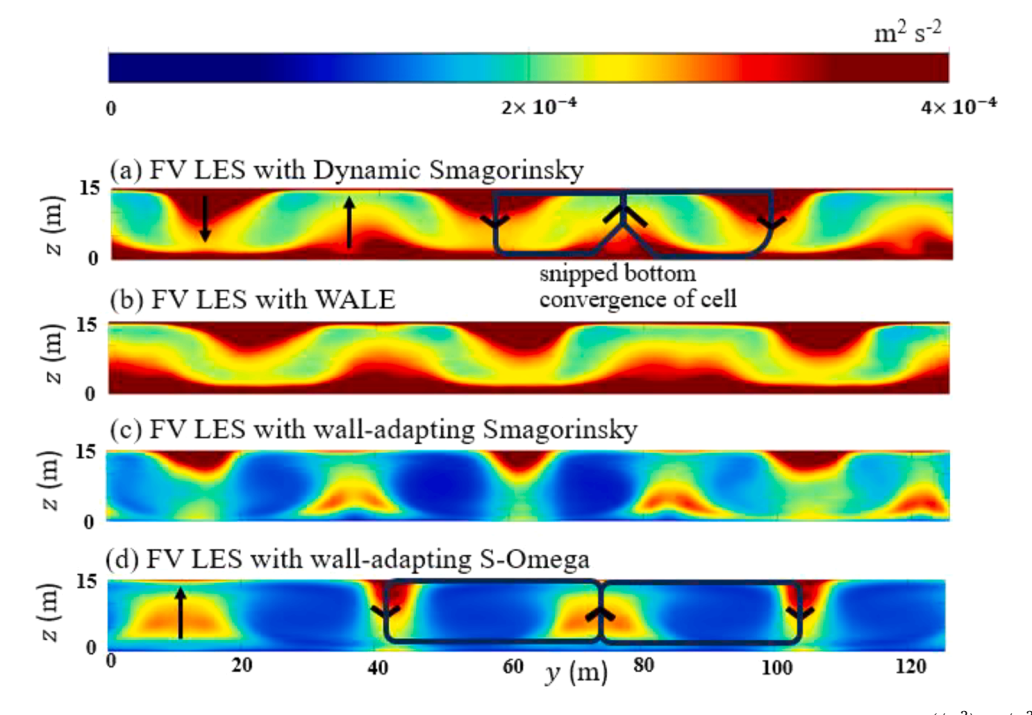
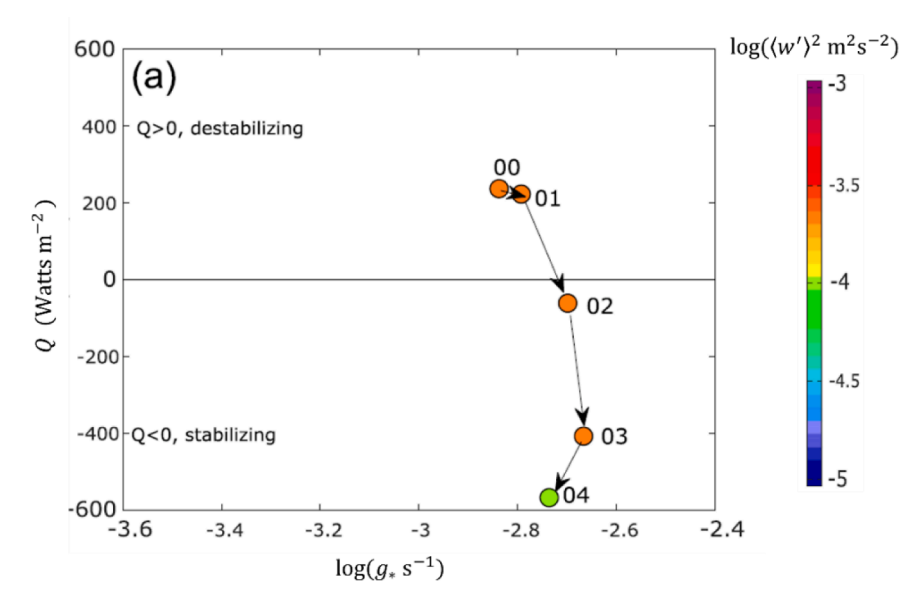
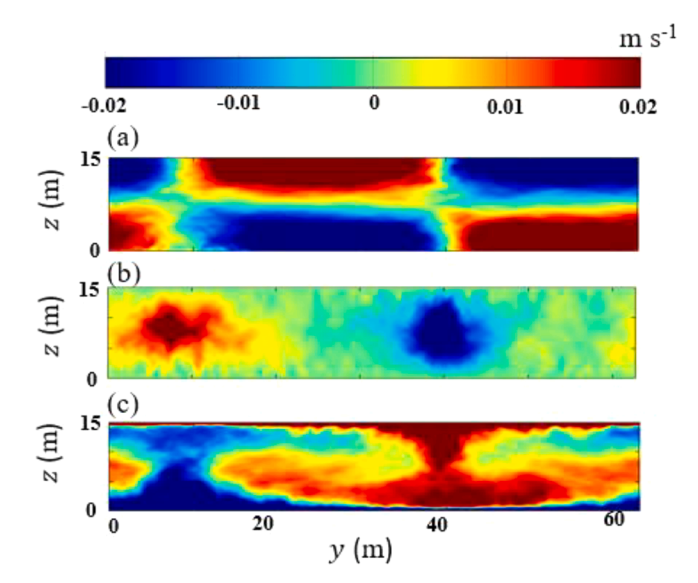


Fig. 16. Resolved turbulent kinetic energy (TKE) at t=30 h. in finite volume (FV) LES. Instantaneous resolved TKE is defined as  $(\langle u'^2 \rangle_x + \langle v'^2 \rangle_x + \langle w'^2 \rangle_x)/2$  where  $\langle \cdot \cdot \rangle_x$  denotes averaging over the downwind direction.



**Fig. 17.** Data of Gargett [25], illustrating the influence of time-dependent surface buoyancy forcing (in terms of surface heat flux Q) on time-averaged and depth-averaged vertical velocity variance during a full-depth LC event at relatively constant wave forcing (in terms of  $g_*$ ). The inverse time scale  $g_*$  is used by Gargett [25] as a measure of wave forcing. The field measurements displayed here are characterized by relatively constant  $g_*$ , thus relatively constant wave forcing. These results suggest a long turbulence adjustment time scale associated with surface heat flux.



**Fig. 18.** Instantaneous downwind-averaged crosswind (a), vertical (b), and downwind (c) velocity fluctuations over the vertical (z) and crosswind extents (y) of the computational domain with zero surface heat flux. This solution served as initial condition for case 00 with surface heat flux set to Q=205 Watts m<sup>-2</sup>.

averaged over the depth of the water column considered by Gargett [25]. Note that Gargett [25] measurements span the water column between 1.4 and 12 m above the bottom of the water column due to limitations of the instrumentation.

During the first 8 h of simulation, when the surface heat flux decreased stepwise from 205 to -400 Watts  $\rm m^{-2}$ , as described above, the peak vertical velocity variance stayed at about 1.8 cm² s²² (Fig. 19). Remarkably, following the trend of the field measurements, a delayed response was finally observed in the vertical velocity variance over hours 9 and 10 of continuous stabilizing heat flux as Q dropped from  $\sim -400$  to -600 Watts  $\rm m^{-2}$  resulting in a peak of vertical velocity variance reaching up to  $0.9~\rm cm^2~s^{-2}$ . Such a delayed response is indicative of the importance that LC can have towards the vertical transport in coastal

waters under sustained strong wind and wave forcing.

Surface heating can lead to stably stratified turbulence which can be challenging for LES and related SGS models to represent. The reason for this is that surface heating can greatly dampen the vertical velocity fluctuations relative to the downwind and crosswind velocity fluctuations, leading to what is often referred to as "pancake turbulence". In these situations, the Smagorinsky-based models can lead to overdamping of the vertical velocity fluctuations (e.g. see [39]). However, in the present simulations, the strength of the full-depth Langmuir cell is diminished by the surface heating applied, but not to the point of resulting in "pancake turbulence" as the full-depth cell is still present at the end of the simulation inducing significant downwelling and upwelling (vertical) velocities.

## 6. Summary and conclusions

The performance of various SGS models were investigated in finite volume LES simulations of wind and wave-driven full-depth LC in the coastal ocean. It was found that for a relatively coarse mesh commensurate with wall-modeled LES (coarser than LES with near-wall resolution), the results depend strongly on the SGS model and the near-wall treatment of the SGS eddy viscosity. This was expected given that the full-depth Langmuir cells significantly magnify the TKE in the bottom boundary layer relative to wind-driven flow without LC [14] and the SGS model may or may not represent this elevated turbulence intensity accurately. The wall-adapting S-Omega model possessing a near-wall behavior following RANS turbulence models, and a velocity scale that takes into consideration the rotation or vorticity in LC flows, was found to lead to a full-depth LC structure in good agreement with the cell structure obtained in well-resolved pseudo-spectral LES and field measurements of full-depth LC. The dynamic Smagorinsky and WALE SGS models with the relatively coarse mesh were found to be under-dissipative in the near-wall region leading to an over-prediction of bottom-generated shear turbulence. The latter was deemed as a disruptor of the full-depth LC serving to "snip" the bottom convergences of the cells, leading to weakened upward transport of slow downwind velocity fluid by the upwelling limbs of the cells. The higher near-bottom eddy viscosity provided by the wall-adapting S-Omega model was able to more accurately account for the bottom-generated shear turbulence, enabling a more accurate resolution of the full-depth

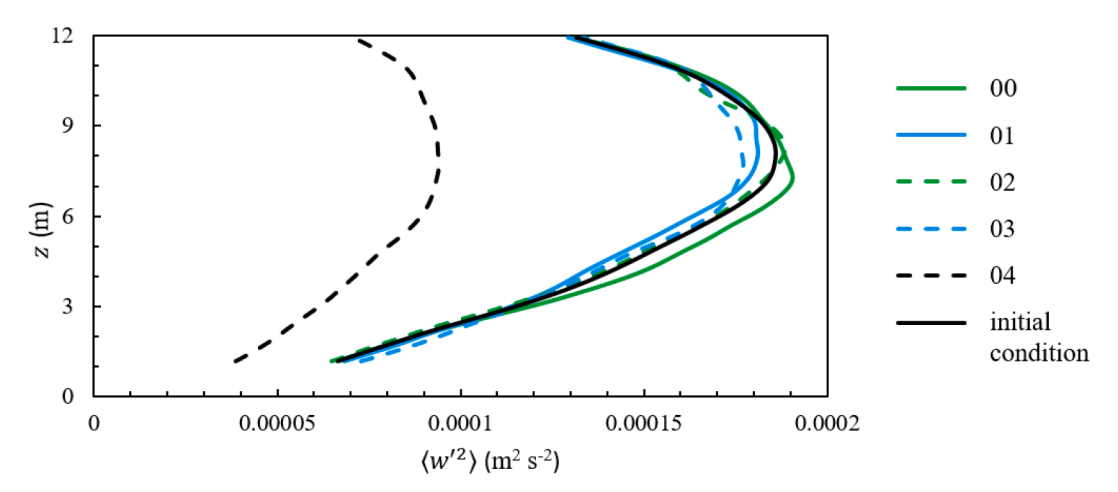


Fig. 19. Resolved vertical velocity variances in LES with surface heat flux.

Table 1 Comparison between LES and field measurements in terms of vertical velocity variance,  $m^2\,s^{-2}$ .

Time spans	Vertical velocity variance in LES	Vertical velocity variance in field measurements of Gargett [25]
00	9.153e-05	~ 2.00e-4
01	9.162e-05	~ 2.00e-4
02	9.137e-05	~ 2.00e-4
03	9.084E-05	~ 2.00e-4
04	5.02861E-05	~ 1.00e-4

LC structure, consistent with pseudo-spectral LES and field measurements.

Based on the positive results obtained with the S-Omega SGS model, finite volume LES with this model was further tested with surface buoyancy. LES of full-depth LC with the S-Omega SGS model was performed with surface cooling and heating corresponding to the diurnal cycle during field measurements of full-depth LC of Gargett [25]. The LES led to good agreement with the field measurements in terms of the temporal evolution of the depth-averaged vertical velocity variance, representative of the strength of the LC. The LES was able to accurately capture the time-response of the full-depth LC to over 6 h of continuous surface heating. It was shown that full-depth LC can be a dominant turbulent structure in the coastal ocean requiring times longer than 6 h in order for its vigorous vertical transport to be significantly suppressed by surface heating.

The results obtained with the finite volume LES with the different SGS models highlight an important interaction between the full-depth Langmuir cells and the bottom-generated shear turbulence mediated by the SGS model. A more detailed analysis of this interaction and mediation would require, for example, a triple decomposition of the flow into the mean component, the full-depth Langmuir cell component, and the smaller turbulent scales. An initial attempt at developing TKE transport equations for each of these components has been made by Martinat et al. [40] and should be continued in the future to better understand the role of the SGS model in the energy transfer across the three components. This analysis should also be informed by energy spectra at various depths of the water column.

As discussed in the Introduction, full-depth LC can contribute significantly to the TKE throughout the water column, observed in low Reynolds number pseudo-spectral LES of Tejada-Martinez and Grosch [14] and corroborated by the infinite Reynolds number simulations of Kukulka et al. (2010, [9]). The Reynolds number independence of full-depth LC suggested by the good agreement between the low-Reynolds (low-Re) number simulations of Tejada-Martinez and Grosch [14] and the field measurements of Gargett and Wells [4], as

identified by Tejada-Martinez et al. [23], further supports this finding. Therefore, findings on the performance of the SGS models and the FVM in full-depth LC flow at low *Re* highlighted in the current study should also be applicable to LES at high (field-scale) Reynolds numbers. Nevertheless, future high Reynolds number LES of full-depth LC should explore not only the performance of the SGS model, but also the performance of the wall model [20,22]. This is important because high Reynolds number simulations of wall-bounded flows assume a weak coupling between the flow structures in the outer boundary layer and the turbulence in the inner layer, which is not the case in flows with full-depth LC.

Future research should also seek to further understand the behavior of the dynamic Smagorinsky and WALE models in finite volume LES of full-depth LC. For example, the scale-invariance assumption required by the dynamic Smagorinsky model may not be valid in the LES conducted here and might need to be reconsidered. In such instances, the dynamic Smagorinsky model can be under-dissipative [41]. Furthermore, the impact of the grid length scale  $\Delta$  in the SGS models should be considered in the future. This length scale was taken as shown in Eq. (11) for the wall-adapting S-Omega and Smagorinsky models, meanwhile it was taken as the cube root of the cell volume for the dynamic Smagorinsky and the WALE models. The length scale in (11) was designed by Shur et al. [19] to depend not only on the grid spacing, but also on the wall distance. Shur et al. [19] showed that (11) leads to significant improvement in the resolved mean velocity over the more traditional cube root of the cell volume expression for  $\Delta$  for wall-resolved LES of turbulent channel flow at  $Re_{\tau} = 395$  with the constant coefficient Smagorinsky model with van Driest damping function.

Ask and Davidson [37] have shown that the BCD advection discretization used in the finite volume LES is less dissipative than second-order upwinding in simulations of the air flow around a generic side mirror of a car. Overall, the BCD scheme provides minimal numerical dissipation within the family of stable advection discretization schemes in the finite volume framework. Thus, it is realistic that the elevated shear turbulence triggered by the impinging of the bottom boundary layer by the downwelling limbs of the Langmuir cells [31] could lead to an unchecked pile-up of energy at the small scales if the SGS model is not sufficiently strong when using the minimal numerically dissipative BCD scheme. This could be the source of the elevated shear turbulence intensity near the bottom of the water column obtained in the simulations with the dynamic Smagorinsky and WALE models. Although replacing the BCD scheme with a more dissipative numerical scheme could address this issue, it could cause an undesired deterioration of resolved Langmuir cell structure.

#### CRediT authorship contribution statement

**Seyedmohammadjavad Zeidi:** Visualization, Validation, Investigation, Formal analysis. **L. Srujana Sarvepalli:** Visualization, Validation. **Andrés E. Tejada-Martínez:** Writing – review & editing, Writing – original draft, Visualization, Supervision, Validation, Resources, Project administration, Methodology, Investigation, Funding acquisition, Formal analysis, Conceptualization.

## Declaration of competing interest

The authors declare that they have no known competing financial interests or personal relationships that could have appeared to influence the work reported in this paper.

## Data availability

Data will be made available on request.

#### Acknowledgment

This research has been made possible by National Science Foundation Grants 1756902 and 1805786.

#### References

- Skyllingstad ED, Denbo DW. An ocean large-eddy simulation of Langmuir circulations and convection in the surface mixed layer. J Geophys Res Oceans 1995;100:8501-22.
- [2] Gargett AE, Wells JR, Tejada-Martínez AE, Grosch CE. Langmuir supercells: a mechanism for sediment resuspension and transport in shallow seas. Science 2004; 306:1925–8 (1979).
- [3] Sinha N. Toward a K-profile parameterization of Langmuir turbulence in shallow coastal shelves. J Phys Oceanogr 2015;45:2869–95.
- [4] Gargett AE, Wells JR. Langmuir turbulence in shallow water. Part 1. Observations. J Fluid Mech 2007;576:27–61.
- [5] Gargett AE, Savidge DK, Wells JR. Anatomy of a Langmuir supercell event. J Mar Res 2014;72:127–63.
- [6] Savidge DK, Gargett AE. Langmuir supercells on the middle shelf of the South Atlantic Bight: 1. Cell structure. J Mar Res 2017;75:49–79.
- [7] Savidge WB, Gargett AE, Jahnke RA, Nelson JR, Savidge DK, Short RT, Voulgaris G. Forcing and dynamics of seafloor-water column exchange on a broad continental shelf. Oceanography 2008;21:179–85.
- [8] Kukulka T, Plueddemann AJ, Sullivan PP. Nonlocal transport due to Langmuir circulation in a coastal ocean. J Geophys Res Oceans 2012:117.
- [9] Kukulka T, Plueddemann AJ, Trowbridge JH, Sullivan PP. The influence of crosswind tidal currents on Langmuir circulation in a shallow ocean. J Geophys Res Oceans 2011:116.
- [10] Edson J, Crawford T, Crescenti J, Farrar T, Frew N, Gerbi G, Helmis C, Hristov T, Khelif D, Jessup A. The coupled boundary layers and air–sea transfer experiment in low winds. Bull Am Meteorol Soc 2007;88:341–56.
- [11] Gerbi GP, Trowbridge JH, Terray EA, Plueddemann AJ, Kukulka T. Observations of turbulence in the ocean surface boundary layer: energetics and transport. J Phys Oceanogr 2009;39:1077–96.
- [12] Deng B-Q, Yang Z, Shen L. Bottom wall shear stress fluctuations in shallow-water Langmuir turbulence. J Fluid Mech 2022;942:A6.

- [13] Deng B-Q, Yang Z, Xuan A, Shen L. Localizing effect of Langmuir circulations on small-scale turbulence in shallow water. J Fluid Mech 2020;893:A6.
- [14] Tejada-Martinez AE, Grosch CE. Langmuir turbulence in shallow water. Part 2. Large-eddy simulation. J Fluid Mech 2007;576:63–108.
- [15] Shrestha K, Anderson W. Coastal Langmuir circulations induce phase-locked modulation of bathymetric stress. Environ Fluid Mech 2020;20:873–84.
- [16] Shrestha K, Anderson W, Tejada-Martínez AE, Kuehl J. Orientation of coastal-zone Langmuir cells forced by wind, wave and mean current at vaiable obliquity. J Fluid Mech 2019;879:716–43.
- [17] Fluent Ansys 2015. "Ansys fluent theory guide, release 15.0." ANSYS, Inc.
- [18] Weller HG, Tabor G, Jasak H, Fureby C. A tensorial approach to computational continuum mechanics using object oriented techniques. Comput Phys 1998;12: 620–31
- [19] Shur ML, Spalart PR, Strelets MK, Travin AK. A hybrid RANS-LES approach with delayed-DES and wall-modelled LES capabilities. Int J Heat Fluid Flow 2008;29: 1638–49
- [20] Bose ST, Park GI. Wall-modeled large-eddy simulation for complex turbulent flows. Annu Rev Fluid Mech 2018;50:535–61.
- [21] Piomelli U. Large-eddy and direct simulation of turbulent flows. In: Proceedings of the 9e conférence annuelle de la société canadienne de cfd CFD2001; 2001.
- [22] Piomelli U, Balaras E. Wall-layer models for large eddy simulations. Annu Rev Fluid Mech 2002;34:349–74.
- [23] Tejada-Martinez AE, Grosch CE, Gargett AE, Polton JA, Smith JA, MacKinnon JA. A hybrid spectral/finite-difference large-eddy simulator of turbulent processes in the upper ocean. Ocean Model 2009;30:115–42 (Oxf).
- [24] Craik ADD, Leibovich S. A rational model for Langmuir circulations. J Fluid Mech 1976;73:401–26.
- [25] Gargett AE. Forcing space: an alternative to regime diagrams for predicting characteristics of turbulence in the ocean surface mixing layer. J Phys Oceanogr 2022;52:519–35.
- [26] Pope SB. Turbulent flows. Cambridge University Press; 2000.
- [27] Piomelli U, Moin P, Ferziger JH. Model consistency in large eddy simulation of turbulent channel flows. Phys Fluids 1988;31:1884–91.
- [28] Lilly DK. A proposed modification of the Germano subgrid-scale closure method. Phys Fluids A Fluid Dyn 1992;4:633–5.
- [29] Nicoud F, Ducros F. Subgrid-scale stress modelling based on the square of the velocity gradient tensor. Flow Turbul Combust 1999;62:183–200.
- [30] Launder B, Spalding D. The numerical computation of turbulent flows. Comput Methods Appl Mech Eng 1974;3:269–89.
- [31] Tejada-Martinez AE, Grosch CE, Sinha N, Akan C, Martinat G. Disruption of the bottom log layer in large-eddy simulations of full-depth Langmuir circulation. J Fluid Mech 2012;699:79–93.
- [32] Launder BE, Spalding DB. The numerical computation of turbulent flows. Comput Methods Appl Mech Eng 1974;3:269–89.
- [33] Darwish M, Sraj I, Moukalled F. A coupled finite volume solver for the solution of incompressible flows on unstructured grids. J Comput Phys 2009;228:180–201.
- [34] Patankar SV. Numerical heat transfer and fluid flow. New York: CRC Press; 1980.
- [35] Leonard BP. The ultimate conservative difference scheme applied to unsteady onedimensional advection. Comput Methods Appl Mech Eng 1991;88:17–74.
- [36] Moukalled F, Mangani L, Darwish M. The finite volume method in computational fluid dynamics. Springer International Publishing Switzerland; 2016.
- [37] Ask J, Davidson L. A numerical investigation of the flow past a generic side mirror and its impact on sound generation. J Fluids Eng 2009;131:161102. -1.
- [38] Thorpe SA. Langmuir circulation. Annu Rev Fluid Mech 2004;36:55-79.
- [39] Sato T, Katayama T, Sato K. Test of large-eddy simulation models for homogeneous-shear turbulence in stratification. J Mar Sci Technol 2006;11: 165–82.
- [40] Martinat G, Grosch CE, Gatski TB. Modeling of Langmuir circulation: triple decomposition of the Craik-Leibovich model. Flow Turbul Combust 2013;92: 395-411
- [41] Porte-Agel F, Meneveau C, Parlange MB. A scale-dependent dynamic model for large-eddy simulation: application to a neutral atmospheric boundary layer. J Fluid Mech 2000;415:261–84.